Master in Theoretical Physics
Utrecht University

Strain Engineering in Graphene and Kagomé Materials

Student:
Matteo Massaro

Supervisor:
Dr. Lars Fritz

Year 2022-2023

Abstract

Since its first synthesis, graphene has opened new exciting research prospects in the context of solid state physics. Despite the simplicity of its structure, this material hosts a rich variety of phenomena and physical properties. In particular, in the low energy limit, it exhibits massless Dirac fermions, typical of 2D Weyl semimetals. However, the semimetallic nature of graphene is generally detrimental for the realization of electronic devices. Therefore it reveals important to find ways to generate a gap in its band structure. In this thesis, employing a tight-binding description, we review the well-known graphene model and the possibility of engineering a spectral gap by applying mechanical strain to its honeycomb structure. This serves as a blueprint to generalize the discussion to the kagomé systems, a novel class of 2D Weyl semimetals for which we construct the effective Dirac theory and classify all the possible mass terms based on the symmetries they preserve or break.

Acknowledgments

I would like to start by expressing my sincere gratitude to my supervisor dr. Lars Fritz who guided me for the entire duration of this thesis project. His knowledge and passion have certainly made this experience valuable and enjoyable.

I would also like to thank Simone, Mikael and Emanuele for the precious discussions and support.

My gratitude goes also to all of my fellow physics students who took part in this journey with me. In particular to Vittorio, with whom I shared both deep reflections and moments of genuine lightheartedness.

Last but not least, my profound gratefulness goes to my family. To my father and my uncle, who supported and guided me with wisdom and patience, making me the person I am today. To my mother and my two sisters for their unconditional love and affection. And finally to my grandmother, who was the first to stimulate my curiosity and critical sense when I was a child and understands me better than anyone else.

Contents

Chapter 1

Introduction

"We are all in the depths of a cave, chained by our ignorance, by our prejudices, and our weak senses reveal to us only shadows. If we try to see further, we are confused; we are unaccustomed. But we try. This is science."

— Carlo Rovelli, Reality is not what it seems.

1.1 Overview and Outline

Solid state physics is certainly one of the richest branches of condensed matter physics. The variety of its phenomena has attracted an increasingly growing interest, both from a theoretical point of view and for the wide range of technological applicability.

Of central importance in its context is the study of the conduction properties of solids. This is encoded in the band structure, which represents the electronic energy distribution in momentum space and leads to a natural classification of the phases of the materials [1].

In the band structure we distinguish the valence and conduction bands, located respectively below and above the Fermi level. At absolute zero temperature, the valence band is filled with electrons bounded to individual atoms. The migration of these electrons towards the upper conduction band is what determines conductivity, and the difficulty or ease to generate this flow provides a criteria of classification.
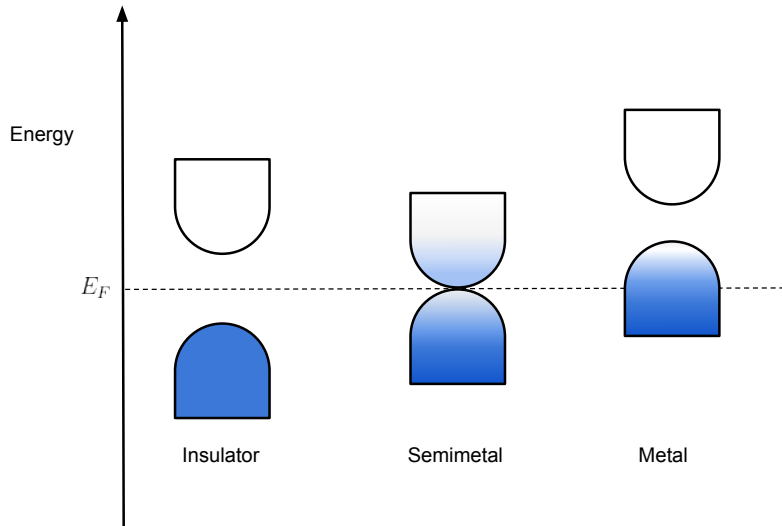
Figure 1.1: Electronic states in insulators, semimetals and insulators. E_F is the Fermi level. The width of the bands encodes the density of states for each corresponding energy. The shade represents the Fermi-Dirac distribution (blue: all states filled, white: no state filled). Adapted from [8].

In particular, if the highest valence band and the lowest conduction band are separated by an energy gap, we call the material insulator. On the contrary if the spectrum is gap-less with a non-zero density of states at the Fermi level the material is said to be a metal. There exists another possible category represented by semimetals: these materials are gapless but with a vanishing density of states at the Fermi level. [1]

A special class of solids that has particularly intrigued the science community in the last years is represented by two-dimensional materials. The outbreak of this interest has been certainly fueled by the discovery of graphene in 2004 [13]. This material consists of carbon atoms arranged in a honeycomb pattern, and it has been first synthesized by isolating a single layer of atoms from three-dimensional graphite.

From a conduction point of view graphene is a gapless semimetal, having a vanishing density of states at the Fermi level. The Fermi surface presents six double cones where the the valence and conduction bands touch each other [20]. These special points are called Weyl nodes (or also Dirac points) and the energy dispersion in their proximity is linear in momentum.

---

[1] In materials science there is a distinction between semimetals and semiconductors. As we said, the former have no gap and vanishing density of states at the Fermi energy, whereas the latter present a small gap ($< 4eV$). However in this thesis we will use the two denominations interchangeably.
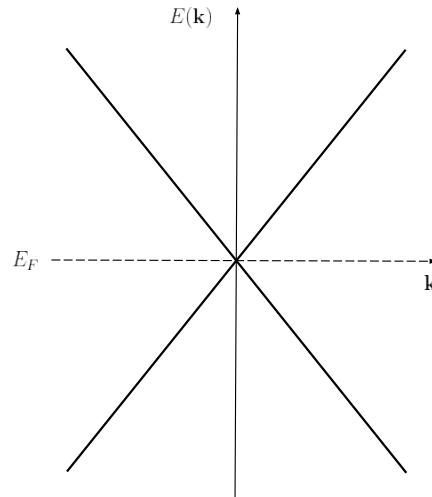
Figure 1.2: Linear energy dispersion near a Weyl node.

This feature, reminiscent of relativistic physics, is what characterizes in general a class of two-dimensional materials called Weyl semimetals [20]. In fact, as we will see, low energy excitations near a node are well described by a massless Dirac Hamiltonian, with the speed of light replaced by the so called Fermi velocity v_F (dependent on the material). In graphene its value is approximately

$$v_F = 10^6 m/s \approx \frac{c}{300}. \tag{1.1}$$

Massless Dirac fermions can therefore be realized in graphene, providing new ways to investigate the scattering properties of Dirac particles. This is an outstanding feature, which creates a bridge between high energy phenomena and low energy systems. A famous example of it is the realization of the Klein paradox [7].

Despite the numerous remarkable properties of graphene, a gapless spectrum can be detrimental in many circumstances and device applications, where completely hindering charge flow is desirable. Therefore a relevant question to address is how to induce a gap at the Dirac points. This can be achieved by introducing a mass in the two-dimensional Dirac Hamiltonian. All the graphene mass terms can be found in the literature, and have been classified based on the symmetries they preserve or break [2].
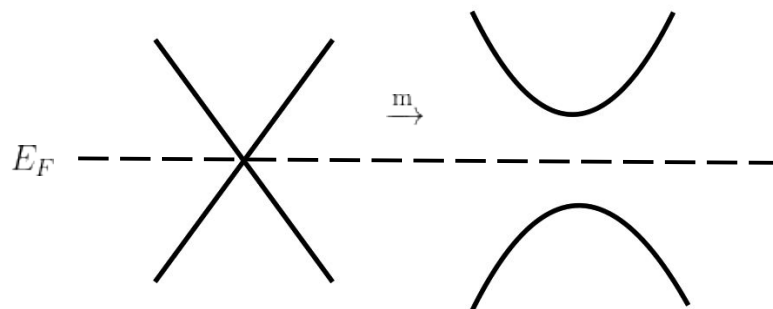

Figure 1.3: Modification of the spectrum due to the introduction of mass in the Dirac Hamiltonian.

On the other hand it has been shown that one possible way to engineer a gap in graphene is by applying strain to the material [18]. However the structure of the Dirac cones is robust, and a strain threshold has to be exceeded in order to produce a gap. This threshold depends on the particular strain employed and is it generally large. Nevertheless this is still applicable due to the remarkable elastic properties of graphene: it is in fact one of the strongest material ever measured, being able to sustain reversible elastic deformations up to 25% [16].

Another more recently discovered class of two-dimensional Weyl semimetals that has drawn notable interest is represented by systems on the kagomé lattice [5]. These novel materials present an hexagonal structure, with the atoms placed on the edges of the hexagon rather than on the vertices, as in graphene. It follows that the unit cell is composed of three different sub-lattices. As we will show, the kagomé band structure, analogously to graphene, shows emergent mass-less Dirac fermions. However, an exhaustive list of its mass terms with the corresponding symmetry classification is lacking in the literature.

The aim of the first part of this thesis is to fill this gap. Employing a tight-binding description of the kagomé lattice, we explicitly extract the underlying Dirac theory. We then proceed to determine all the mass terms, and provide their symmetry classification.

In the second part, utilizing linear elasticity theory, strain is introduced in the model. We begin by studying it in the case of graphene. In particular, the connection between the strain-induced gap and the general mass terms of the Dirac theory is explored. We then extend the discussion to the kagomé case to investigate if this remains a viable method to generate a bulk gap.

1.2   Graphene Tight-binding Model

Let us begin by briefly reviewing the tigh-binding description of graphene. This will serve as a useful reference for the following, where we will extend this model to the kagomé lattice and introduce elastic deformations in the theory.

The second quantized tight-binding Hamiltonian with nearest neighbor hopping reads

$$\mathbf{H} = -t \sum_{\langle i,j \rangle, \sigma} (a_{i,\sigma}^\dagger b_{j,\sigma} + h.c.), \tag{1.2}$$

where a and b are the fermionic quantum operators respectively acting on the two different sub-lattices A, B [12] and satisfying the canonical anti-commutation relations [2]

$$\{ a_\alpha, a_\beta \} = \{ a_\alpha^\dagger, a_\beta^\dagger \} = 0 \quad , \quad \{ a_\alpha, a_\beta^\dagger \} = \delta_{\alpha,\beta} \quad \text{(same for } b\text{)}. \tag{1.3}$$

The latin indices i, j denote the real space positions of the lattice sites and σ labels the electronic spin states $| \uparrow \rangle, | \downarrow \rangle$. The constant t is called hopping parameter and it encodes the probability amplitude for an electron to hop between two neighbouring sites. In the graphene case its value is

$$t = 2.7 \text{eV}. \tag{1.4}$$

---

[2]Here α and β span over all the degrees of freedom of the system. Moreover the two sets of operators a and b anti-commute between each other.

It is possible to consider models in which electronic hops between second nearest neighbours (and even beyond) are also taken into account, however we will neglect those effects in our discussion.
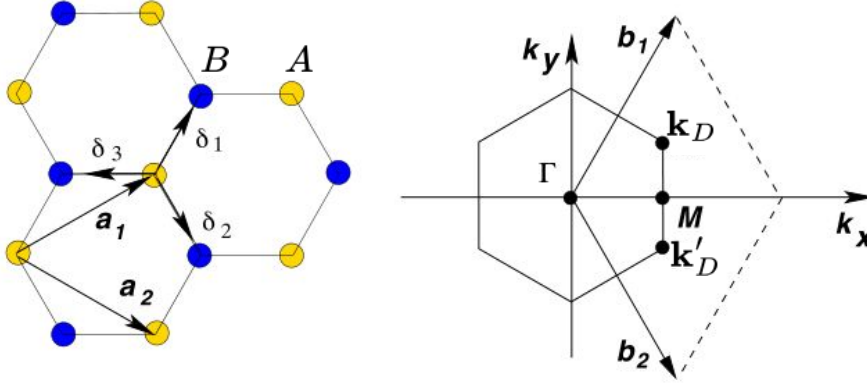

Figure 1.4: Lattice structure of graphene in real space and its first Brillouin zone. b_1 and b_2 are the reciprocal lattice vectors. $\mathbf{K}_D$ and $\mathbf{K}'_D$ indicate the independent Dirac points. (Adapted from [12]).

Given an electron on site $\mathbf{r}_i$ of the A sub-lattice, the three nearest neighbors are found at positions

$$\mathbf{r}_j \in B = \mathbf{r}_i + \boldsymbol{\delta}_{1,2,3} \tag{1.5}$$

with

$$\boldsymbol{\delta}_1 = \frac{a}{2}(1, \sqrt{3})^T \quad , \quad \boldsymbol{\delta}_2 = \frac{a}{2}(1, -\sqrt{3})^T \quad , \quad \boldsymbol{\delta}_3 = -a(1,0)^T. \tag{1.6}$$

The Hamiltonian (1.2) can therefore be rewritten as

$$\mathbf{H} = -t \sum_{i \in A, \sigma, \boldsymbol{\delta}} (a_{i,\sigma}^\dagger b_{i+\boldsymbol{\delta},\sigma} + h.c.). \tag{1.7}$$

We then proceed to Fourier transform the quantum operators:

$$a_i = \frac{1}{\sqrt{N/2}} \sum_{\mathbf{k}} e^{-i\mathbf{k}\cdot\mathbf{r}_i} a_{\mathbf{k}} \quad , \quad a_i^\dagger = \frac{1}{\sqrt{N/2}} \sum_{\mathbf{k}} e^{i\mathbf{k}\cdot\mathbf{r}_i} a_{\mathbf{k}}^\dagger, \tag{1.8}$$

with N the total number of lattice sites (or equivalently $N/2$ the total number of unit cells). Plugging the latter expressions in eq.(1.7) we obtain

$$\mathbf{H} = -t \sum_{i \in A, \sigma, \boldsymbol{\delta}} \sum_{\mathbf{k}, \mathbf{k}'} \frac{1}{N/2} (e^{i(\mathbf{k}-\mathbf{k}')\cdot\mathbf{r}_i} e^{-i\mathbf{k}'\cdot\boldsymbol{\delta}} a_{\mathbf{k}}^\dagger b_{\mathbf{k}'} + h.c.) =$$

$$= -t \sum_{\sigma, \boldsymbol{\delta}, \mathbf{k}} (e^{-i\mathbf{k}\cdot\boldsymbol{\delta}} a_{\mathbf{k}}^\dagger b_{\mathbf{k}} + h.c.) \tag{1.9}$$

where we have made use of the identity

$$\frac{1}{N/2} \sum_{i \in A} e^{i(\mathbf{k}-\mathbf{k}')\cdot\mathbf{r}_i} = \delta_{\mathbf{k},\mathbf{k}'}. \tag{1.10}$$

Finally, we can conveniently cast $\mathbf{H}$ in the form

$$\mathbf{H} = -t \sum_{\mathbf{k},\sigma} \Psi_{\mathbf{k},\sigma}^\dagger H(\mathbf{k}) \Psi_{\mathbf{k},\sigma} \tag{1.11}$$

having defined Ψ the vector of fermionic operators

$$\Psi_{\mathbf{k},\sigma} = \begin{pmatrix} a_{\mathbf{k},\sigma}, & b_{\mathbf{k},\sigma} \end{pmatrix}^T. \tag{1.12}$$

$H(\mathbf{k})$ is the Block Hamiltonian, and has the form

$$H(\mathbf{k}) = \begin{pmatrix} 0 & \sum_{j=1,2,3} e^{-i\mathbf{k}\cdot\boldsymbol{\delta}_j} \\ \sum_j e^{i\mathbf{k}\cdot\boldsymbol{\delta}_j} & 0 \end{pmatrix} := \begin{pmatrix} 0 & \Delta(\mathbf{k}) \\ \Delta^*(\mathbf{k}) & 0 \end{pmatrix}. \tag{1.13}$$

The energy bands are readily found by diagonalizing it:

$$E_\pm = \pm t\sqrt{\Delta(\mathbf{k})\Delta^*(\mathbf{k})} = \sqrt{1 + 4\cos\left(\frac{3}{2}k_x a\right)\cos\left(\frac{\sqrt{3}}{2}k_y a\right) + 4\cos^2\left(\frac{\sqrt{3}}{2}k_y a\right)}, \tag{1.14}$$

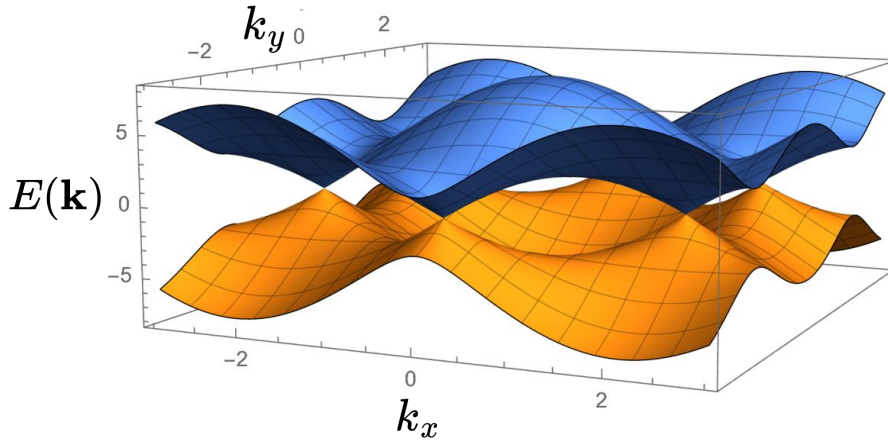where here a indicates the bond length between carbon atoms.

Figure 1.5: Graphene band structure.

1.2.1   Low Energy Expansion

The band structure of graphene, depicted in Fig.(1.5), is characterized by two bands touching each other on a discrete set of points. Therefore if we set the chemical potential μ to zero, such that the Fermi level lies at the junction of the two bands (at $E = 0$), then the material behaves as a semimetal.

In particular within the first Brillouin zone there are six points of contact between the two bands, which incidentally coincide with the corners of the hexagon delimiting the reciprocal unit cell (see Fig1.4). Therefore it follows that only two of them are independent and a possible choice is to consider

$$\mathbf{k}_D = \left(\frac{2\pi}{3a}, \frac{2\pi}{3\sqrt{3}a}\right) \quad , \quad \mathbf{k}'_D = \left(\frac{2\pi}{3a}, -\frac{2\pi}{3\sqrt{3}a}\right). \tag{1.15}$$

These special momentum values are called Dirac points for the following reason: expanding the Block Hamiltonian $H(\mathbf{k})$ around $\mathbf{k}_D$ up to linear order in momentum yields

$$H(\mathbf{k}_D + \mathbf{q}) \approx \frac{3}{2}at \begin{pmatrix} 0 & q_x + iq_y \\ q_x - iq_y & 0 \end{pmatrix} = v_F(q_x\tau_1 - q_y\tau_2), \tag{1.16}$$

where $\tau_{1,2}$ are the usual Pauli matrices, and v_F is the graphene Fermi velocity

$$v_F = \frac{3}{2}at. \tag{1.17}$$

Eq.(1.16) has indeed the form of a two-dimensional Dirac Hamiltonian, with the velocity of light c replaced by v_F. Analogously the expansion around $\mathbf{k}'_D$ is

$$H(\mathbf{k}'_D + \mathbf{q}) \approx \frac{3}{2}at \begin{pmatrix} 0 & q_x - iq_y \\ q_x + iq_y & 0 \end{pmatrix} = v_F(q_x\tau_1 + q_y\tau_2). \tag{1.18}$$

An Hamiltonian containing both of these expanded blocks effectively describes the low energy excitations of the system:

$$H_{eff} = v_F \begin{pmatrix} 0 & q_x - iq_y & 0 & 0 \\ q_x + iq_y & 0 & 0 & 0 \\ 0 & 0 & 0 & q_x + iq_y \\ 0 & 0 & q_x - iq_y & 0 \end{pmatrix}. \tag{1.19}$$

This is what we call low energy effective theory, and we will reflect more on its construction when discussing it in the kagomé case.

It is convenient to rewrite eq.(1.19) in the form of a tensor product of Pauli matrices:

$$H_{eff} = v_F(\sigma_0 \otimes \tau_1 k_x + \sigma_3 \otimes \tau_2 k_x), \tag{1.20}$$

such that the different degrees of freedom of the system are distinguished. In particular τ acts on the sublattice space, and σ on the so called valley degree of freedom. We can think the latter as a quantum number (just like spin) that labels the states based on their momentum, which can either be close to one or the other Dirac point. The wave function is therefore a spinor with components

$$\psi = \begin{pmatrix} A_+ & B_+ & A_- & B_- \end{pmatrix}^T \tag{1.21}$$

where $\pm$ labels the two different valleys.

Eq.(1.19) is valid for a spinless system. Introducing back this degree of freedom, the full effective theory takes the form

$$H_{eff} = v_F(s_0 \otimes \sigma_0 \otimes \tau_1 k_x + s_0 \otimes \sigma_3 \otimes \tau_2 k_x), \tag{1.22}$$

where s are the Pauli matrices acting on the spin degree of freedom. The corresponding spinor reads

$$\psi = \begin{pmatrix} A_{+\uparrow} & B_{+\uparrow} & A_{-\uparrow} & B_{-\uparrow} & A_{+\downarrow} & B_{+\downarrow} & A_{-\downarrow} & B_{-\downarrow} \end{pmatrix}^T. \tag{1.23}$$

1.3   Unitary and Anti-unitary Symmetries

We conclude this introductory chapter with a review of unitary and anti-unitary symmetries, which will be used later in the classification of the kagomé mass terms.

Unitary symmetries are a powerful tool that can be used to greatly simplify the study of a system. A great example that we have already exploited is translational invariance, which enabled us to block diagonalize the Hamiltonian in momentum space. This is in fact a general feature: if the one-particle Hamiltonian H commutes with a unitary transformation U, we can find a basis in which both H and U are block diagonal. This drastically reduces the dimensionality of the problem, as we only need to study the individual sub-blocks of the Hamiltonian. Once we have exhausted all the possible unitary symmetries of the system, we can further find anti-unitary transformations that either commute or anti-commute with the individual

blocks of H. This are given by Time reversal ($\mathcal{T}$) and Charge ($\mathcal{C}$) symmetries. We can further combine them to obtain Sublattice symmetry ($\mathcal{S}$) as

$$\mathcal{S} = \mathcal{T} \cdot \mathcal{C}, \tag{1.24}$$

which turns out to be unitary, but anti-commutes with H.

Before analyzing each of them, we need to define formally what we mean by symmetry. The most fundamental definition is given in the contex of second quantization [3]. Let us then consider a generic (non interacting) second quantized Hamiltonian, which has the general form

$$\hat{\mathbf{H}} = \sum_{A,B} \hat{\Psi}_A^\dagger H_{A,B} \Psi_B. \tag{1.25}$$

with the fermionic creation and anhilation operators that satisfy the canonical anti-commutation relations

$$\{\ \Psi_A, \Psi_B^\dagger\ \} = \delta_{A,B} \quad , \quad \{\ \Psi_A, \Psi_B\ \} = \{\ \Psi_A^\dagger, \Psi_B^\dagger\ \} = 0. \tag{1.26}$$

Here A and B span over all the degrees of freedom of the system.

A symmetry is then defined as a linear transformation of the fermionic operators, that commutes with the second-quantized Hamiltonian and preserves the canonical relations (1.26). In particular:

$$\hat{\Psi}_A \to \hat{\Psi}_A' = \sum_B U_{A,B} \hat{\Psi}_B := \hat{\mathcal{U}} \hat{\Psi}_A \hat{\mathcal{U}}^{-1} \tag{1.27}$$

$$\hat{\Psi}_A^\dagger \to \hat{\Psi}_A'^\dagger = \sum_B \hat{\Psi}_B^\dagger U_{A,B}^* := \hat{\mathcal{U}} \hat{\Psi}_A^\dagger \hat{\mathcal{U}}^{-1} \tag{1.28}$$

where $\hat{\mathcal{U}}$ is the second quantized operator of the symmetry (which can either be unitary or anti-unitary), while U is a unitary matrix (U_{AB} is a collection of numbers). [3] By definition this is a symmetry if it commutes with the second-quantized Hamiltonian

$$\hat{\mathcal{U}} \cdot \hat{\mathbf{H}} \cdot \hat{\mathcal{U}}^{-1} = \hat{\mathbf{H}}. \tag{1.29}$$

We particularly put emphasis on equation (1.29), which is really what is meant by symmetry. This will be in fact true for time reversal, charge and sublattice symmetries:

$$\hat{\mathcal{T}} \cdot \hat{\mathbf{H}} \cdot \hat{\mathcal{T}}^{-1} = \hat{\mathbf{H}} \quad , \quad \hat{\mathcal{C}} \cdot \hat{\mathbf{H}} \cdot \hat{\mathcal{C}}^{-1} = \hat{\mathbf{H}} \quad , \quad \hat{\mathcal{S}} \cdot \hat{\mathbf{H}} \cdot \hat{\mathcal{S}}^{-1} = \hat{\mathbf{H}}. \tag{1.30}$$

However we have to be careful, since this commutation relation applies to the second-quantized Hamiltonian. The corresponding condition on the one-particle Hamiltonian H is found by plugging inside (1.29) the general form for the second quantized Hamiltonian (1.25). As we will see the resulting symmetry condition on H will be different depending on the particular symmetry. In fact, H can either commute (as in the case of $\mathcal{T}$) or anti-commute (as in the case of $\mathcal{C}$) with the symmetry operator.

1.3.1 Time Reversal

Let us now discuss more specifically time reversal. We begin by providing a review of this anti-unitary symmetry using first quantization language [17]. It will then be instructive to also generalize it in the second quantization formalism.

---

[3]The fact that U is unitary follows from the requirement that (1.26) are preserved under $\hat{\mathcal{U}}$.

1.3.1.1   Time reversal in first quantization

Time reversal is the fundamental transformation

$$\mathcal{T} : t \to -t, \tag{1.31}$$

that reverses the dynamic of a system. As anticipated, the quantum mechanical operator that implements this discrete symmetry is anti-unitary. To prove this important property, we consider a system described by a state $|\alpha\rangle$ at $t = 0$. After an infinitesimal time interval δt, the evolved state is simply

$$|\alpha, \delta t\rangle = (1 - \frac{i\hat{H}\delta t}{\hbar})|\alpha\rangle. \tag{1.32}$$

On the other hand, if we first time-reverse the initial state, and then look at its evolution, after δt we end up with

$$(1 - \frac{i\hat{H}\delta t}{\hbar})\mathcal{T}|\alpha\rangle. \tag{1.33}$$

If the system is time reversal invariant, we expect that the following holds

$$(1 - \frac{i\hat{H}\delta t}{\hbar})\mathcal{T}|\alpha\rangle = \mathcal{T}|\alpha, -\delta t\rangle \implies (1 - \frac{i\hat{H}\delta t}{\hbar})\mathcal{T}|\alpha\rangle = \mathcal{T}(1 + \frac{i\hat{H}\delta t}{\hbar})|\alpha\rangle. \tag{1.34}$$

This is intuitively understood in the case where $|\alpha\rangle = |\mathbf{p}\rangle$ as in Fig.(1.6).
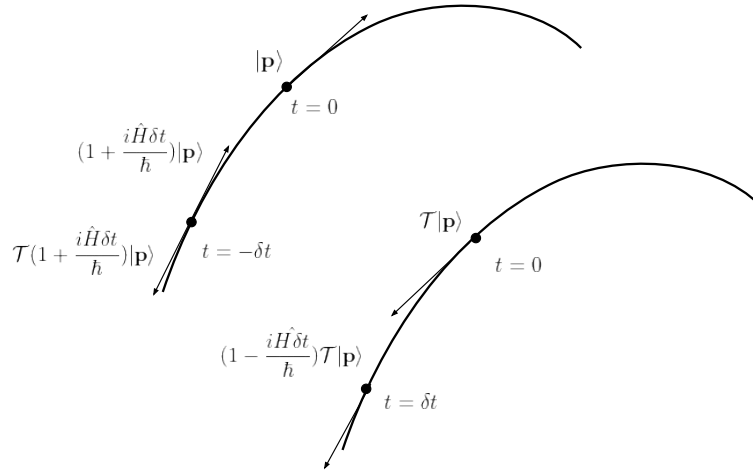
Figure 1.6: Time reversal of momentum states.

It follows that

$$-iH\mathcal{T} = \mathcal{T}iH. \tag{1.35}$$

At this point, a simplification of the imaginary unit would yield the contradictory result

$$\{ H, \mathcal{T} \} = 0. \tag{1.36}$$

This, in fact, would mean that for each energy eigenstate $|E\rangle$ there exists another, obtained by time reversing $|E\rangle$, with opposite energy

$$H\mathcal{T}|E\rangle = -\mathcal{T}H|E\rangle = -E\mathcal{T}|E\rangle. \tag{1.37}$$

Clearly this is a nonphysical result, which suggests that $\mathcal{T}$ must instead be anti-unitary

$$\mathcal{T}i\mathcal{T}^{-1} = -i, \tag{1.38}$$

and therefore

$$[H, \mathcal{T}] = 0. \tag{1.39}$$

It is easy to show that an anti-unitary operator can be expressed as a composition of complex conjugation and a unitary transformation

$$\mathcal{T} = U_{\mathcal{T}} \circ \mathcal{K}. \tag{1.40}$$

In particular the operator $\mathcal{K}$ acts on a generic state by changing the expansion coefficients with their complex conjugate and leaving the basis states untouched

$$\mathcal{K} \sum_i \alpha_i |i\rangle = \sum_i \alpha_i^* |i\rangle. \tag{1.41}$$

The action of time reversal on a generic operator can therefore be written as

$$\hat{A} \to \mathcal{T}\hat{A}\mathcal{T}^{-1} = U_{\mathcal{T}}\hat{A}^* U_{\mathcal{T}}^{-1}. \tag{1.42}$$

using this, we can rewrite the condition (1.39) as

$$U_{\mathcal{T}} H^* U_{\mathcal{T}}^{-1} = H. \tag{1.43}$$

Another important property is that hermitian operators can be either odd or even under the action of $\mathcal{T}$

$$\mathcal{T}\hat{A}\mathcal{T}^{-1} = \pm\hat{A}, \tag{1.44}$$

being a direct consequence of the anti-unitarity.

In particular for position, momentum and spin it is reasonable to expect

$$\mathcal{T}\mathbf{x}\mathcal{T}^{-1} = \mathbf{x} \quad , \quad \mathcal{T}\mathbf{p}\mathcal{T}^{-1} = -\mathbf{p} \quad , \quad \mathcal{T}\boldsymbol{s}\mathcal{T}^{-1} = -\boldsymbol{s}. \tag{1.45}$$

From the first two relations, it becomes immediately clear that time reversal must indeed be anti-unitary. If that was not the case, the canonical commutation relations will in fact not be preserved by the transformation.

1.3.1.2   Time reversal in second quantization

The action of time reversal in second quantization is given by [3]

$$\mathcal{T}\hat{\Psi}_A\mathcal{T}^{-1} = \sum_B (U_{\mathcal{T}})_{AB}\hat{\Psi}_B \quad , \quad \mathcal{T}\hat{\Psi}_A^\dagger\mathcal{T}^{-1} = \sum_B \hat{\Psi}_B^\dagger(U_{\mathcal{T}})_{AB}^* \quad , \quad \mathcal{T}i\mathcal{T} = -i, \tag{1.46}$$

where $U_{\mathcal{T}}$ is a unitary matrix. By definition, a system is time reversal invariant if the second-quantized Hamiltonian is symmetric

$$\mathcal{T} \cdot \hat{\mathbf{H}} \cdot \mathcal{T}^{-1} = \hat{\mathbf{H}}. \tag{1.47}$$

If we plug the generic form of $\hat{\mathbf{H}}$ (given by eq.(1.25)) in eq.(1.47), we can determine the corresponding symmetry condition on the one-particle Hamiltonian H:

$$\mathcal{T}\hat{\mathbf{H}}\mathcal{T}^{-1} = \sum_{A,B} \mathcal{T}\Psi_A^\dagger \mathcal{T}^{-1}\mathcal{T}H_{AB}\mathcal{T}^{-1}\mathcal{T}\Psi_B\mathcal{T}^{-1} =$$

$$= \sum_{A,B}\sum_{C,D} \Psi_C^\dagger (U_\mathcal{T})_{AC}^* H_{AB}^* (U_\mathcal{T})_{BD}\Psi_D = \hat{\mathbf{H}} =$$

$$= \sum_{CD} \Psi_C^\dagger H_{CD}\Psi_D. \tag{1.48}$$

It follows that the system is time reversal symmetric if the one-particle Hamiltonian satisfies

$$U_\mathcal{T}^\dagger H^* U_\mathcal{T} = H. \tag{1.49}$$

This is indeed equivalent to the condition of eq.(1.43), determined by using first quantization.

It is useful to also find the symmetry condition of the one-particle Hamiltonian in momentum space, which reads

$$\mathcal{T}H(\mathbf{k})\mathcal{T}^{-1} = H(-\mathbf{k}) \implies U_\mathcal{T}H^*(\mathbf{k})U_\mathcal{T}^{-1} = H(-\mathbf{k}). \tag{1.50}$$

Chapter 2

Kagomé Lattice

In this chapter we generalize the previous discussion of graphene to the kagomé lattice. We begin by constructing the corresponding tight-binding model and building the effective theory near the Dirac points. As in graphene, this will be described by a massless Dirac Hamiltonian, for which we determine the possible mass terms with their corresponding symmetry classification.

2.1 Tight-binding Model

Let us start by writing the tight binding model on the kagomé lattice. The Hamiltonian, with nearest neighbor hopping parameter t, reads [5]

$$\mathbf{H} = -t \sum_{<i,j,l>,\sigma} (a_{i,\sigma}^{\dagger} b_{j,\sigma} + a_{i,\sigma}^{\dagger} c_{l,\sigma} + b_{j,\sigma}^{\dagger} c_{l,\sigma} + h.c.), \tag{2.1}$$

where a, b, c are the quantum operators acting respectively on the three different sublattices. The indices i, j, l indicate the real space position of the lattice sites and σ is the spin label.
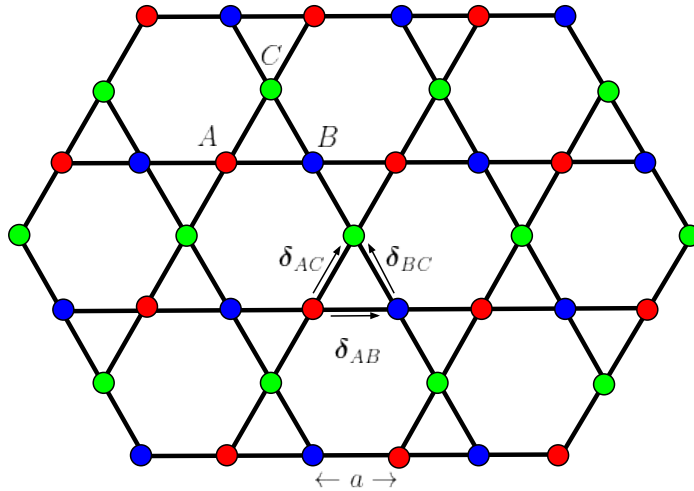

Figure 2.1: Kagomé real space lattice structure. Adapted from [5].

Let us now consider a generic site i, belonging to the A sublattice, at position

r_i. It follows that the positions of the nearest neighbouring sites are

$$\mathbf{r}_j \in B = \mathbf{r}_i \pm \boldsymbol{\delta}_{AB}$$
$$\mathbf{r}_l \in C = \mathbf{r}_i \pm \boldsymbol{\delta}_{AC} \tag{2.2}$$

with

$$\boldsymbol{\delta}_{AB} = a(1,0)^T \quad , \quad \boldsymbol{\delta}_{AC} = \frac{a}{2}(1,\sqrt{3})^T. \tag{2.3}$$

The Hamiltonian can then be rewritten as

$$\mathbf{H} = -t\sum_{i\in A}(a_i^\dagger b_{i+\delta_{AB}}+a_i^\dagger b_{i-\delta_{AB}}+a_i^\dagger c_{i+\delta_{AC}}+a_i^\dagger c_{i-\delta_{AC}}+b_{i+\delta_{AB}}^\dagger c_{i+\delta_{AC}}+b_{i-\delta_{AB}}^\dagger c_{i-\delta_{AC}}+h.c) \tag{2.4}$$

where we have dropped the spin index σ for convenience.

We now make use of the transformation laws for the creation and anihilation operators from real to momentum space

$$a_i^\dagger = \frac{1}{\sqrt{\frac{N}{3}}}\sum_{\mathbf{k}}e^{-i\mathbf{k}\cdot\mathbf{r}_i}a_{\mathbf{k}}^\dagger$$
$$a_i = \frac{1}{\sqrt{\frac{N}{3}}}\sum_{\mathbf{k}}e^{i\mathbf{k}\cdot\mathbf{r}_i}a_{\mathbf{k}}^\dagger. \tag{2.5}$$

with N the total number of lattice sites. Plugging these into eq.(2.4) yields

$$\mathbf{H} = -t\sum_{i\in A}\frac{1}{N/3}\sum_{\mathbf{k},\mathbf{k}'}(e^{i(\mathbf{k}-\mathbf{k}')\cdot\mathbf{r}_i}e^{i\mathbf{k}\cdot\boldsymbol{\delta}_{AB}}a_{\mathbf{k}'}^\dagger b_{\mathbf{k}}+e^{i(\mathbf{k}-\mathbf{k}')\cdot\mathbf{r}_i}e^{-i\mathbf{k}\cdot\boldsymbol{\delta}_{AB}}a_{\mathbf{k}'}^\dagger b_{\mathbf{k}}+e^{i(\mathbf{k}-\mathbf{k}')\cdot\mathbf{r}_i}e^{i\mathbf{k}\cdot\boldsymbol{\delta}_{AC}}a_{\mathbf{k}'}^\dagger c_{\mathbf{k}}+$$

$$+e^{i(\mathbf{k}-\mathbf{k}')\cdot\mathbf{r}_i}e^{-i\mathbf{k}\cdot\boldsymbol{\delta}_{AC}}a_{\mathbf{k}'}^\dagger c_{\mathbf{k}}+e^{i(\mathbf{k}-\mathbf{k}')\cdot\mathbf{r}_i}e^{-i\mathbf{k}'\cdot\boldsymbol{\delta}_{AB}}e^{i\mathbf{k}\cdot\boldsymbol{\delta}_{AC}}b_{\mathbf{k}'}^\dagger c_{\mathbf{k}}+e^{i(\mathbf{k}-\mathbf{k}')\cdot\mathbf{r}_i}e^{i\mathbf{k}'\cdot\boldsymbol{\delta}_{AB}}e^{-i\mathbf{k}'\cdot\boldsymbol{\delta}_{AC}}b_{\mathbf{k}'}^\dagger c_{\mathbf{k}}+h.c.) \tag{2.6}$$

which using

$$\sum_{i\in A}\frac{1}{N/3}e^{i(\mathbf{k}-\mathbf{k}')\cdot\mathbf{r}_i} = \delta_{\mathbf{k},\mathbf{k}'} \tag{2.7}$$

becomes

$$\mathbf{H} = -t\sum_{\mathbf{k}}(e^{i\mathbf{k}\cdot\boldsymbol{\delta}_{AB}}a_{\mathbf{k}}^\dagger b_{\mathbf{k}}+e^{-i\mathbf{k}\cdot\boldsymbol{\delta}_{AB}}a_{\mathbf{k}}^\dagger b_{\mathbf{k}}+e^{i\mathbf{k}\cdot\boldsymbol{\delta}_{AC}}a_{\mathbf{k}}^\dagger c_{\mathbf{k}}+e^{-i\mathbf{k}\cdot\boldsymbol{\delta}_{AC}}a_{\mathbf{k}}^\dagger c_{\mathbf{k}}+$$

$$+e^{i\mathbf{k}\cdot(\boldsymbol{\delta}_{AC}-\boldsymbol{\delta}_{AB})}b_{\mathbf{k}}^\dagger c_{\mathbf{k}}+e^{i\mathbf{k}\cdot(\boldsymbol{\delta}_{AB}-\boldsymbol{\delta}_{AC})}b_{\mathbf{k}}^\dagger c_{\mathbf{k}}+h.c.) =$$

$$= -t\sum_{\mathbf{k}}(2\cos{(\mathbf{k}\cdot\boldsymbol{\delta}_{AB})}a_{\mathbf{k}}^\dagger b_{\mathbf{k}}+2\cos{(\mathbf{k}\cdot\boldsymbol{\delta}_{AC})}a_{\mathbf{k}}^\dagger c_{\mathbf{k}}+2\cos{((\boldsymbol{\delta}_{AC}-\boldsymbol{\delta}_{AB})\cdot\mathbf{k})}b_{\mathbf{k}}^\dagger c_{\mathbf{k}}+h.c.) \tag{2.8}$$

where for the following we define $\boldsymbol{\delta}_{BC} := \boldsymbol{\delta}_{AC} - \boldsymbol{\delta}_{AB} = \frac{a}{2}(-1,\sqrt{3})^T$.

The final expression in eq.(2.8) can be conveniently rearranged as

$$\mathbf{H} = -2t\sum_{k,\sigma}\Psi_\sigma^\dagger(\mathbf{k})\begin{pmatrix} 0 & \cos{(\mathbf{k}\cdot\boldsymbol{\delta}_{AB})} & \cos{(\mathbf{k}\cdot\boldsymbol{\delta}_{AC})} \\ \cos{(\mathbf{k}\cdot\boldsymbol{\delta}_{AB})} & 0 & \cos{(\mathbf{k}\cdot\boldsymbol{\delta}_{BC})} \\ \cos{(\mathbf{k}\cdot\boldsymbol{\delta}_{AC})} & \cos{(\mathbf{k}\cdot\boldsymbol{\delta}_{BC})} & 0 \end{pmatrix}\Psi_\sigma(\mathbf{k}) = \sum_{k,\sigma}\Psi_\sigma^\dagger(\mathbf{k})H(\mathbf{k})\Psi_\sigma(\mathbf{k}) \tag{2.9}$$

with $\Psi(\mathbf{k}) = \begin{pmatrix} a_\sigma(\mathbf{k}) & b_\sigma(\mathbf{k}) & c_\sigma(\mathbf{k}) \end{pmatrix}^T$ the vector of quantum operators, and $H(\mathbf{k})$ the Block Hamiltonian. The energy bands are then determined by diagonalizing $H(\mathbf{k})$

$$\begin{cases} E_{1,2} = t(1 \pm \sqrt{3 + 2\sum_j \cos(2\mathbf{k} \cdot \boldsymbol{\delta}_j)}) \\ E_3 = -2t \end{cases} \tag{2.10}$$

with $\boldsymbol{\delta}_j = (\boldsymbol{\delta}_{AB}, \boldsymbol{\delta}_{AC}, \boldsymbol{\delta}_{BC})$.
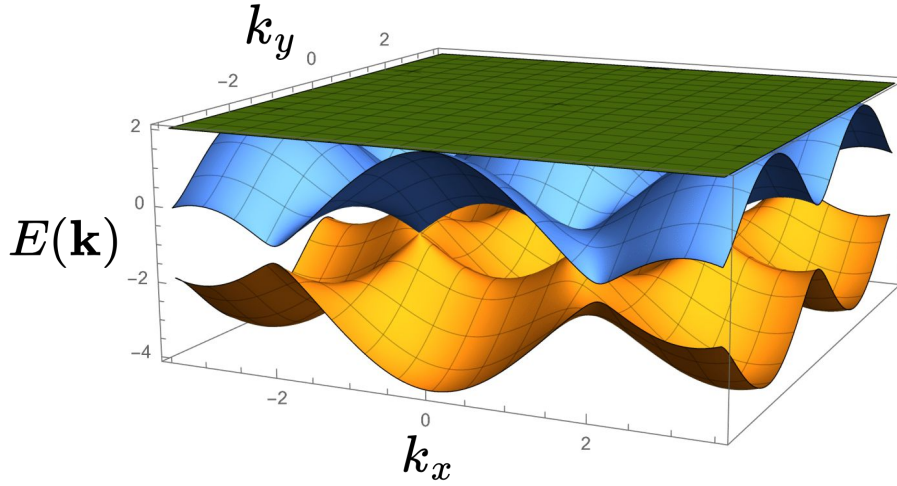

Figure 2.2: Kagomé energy bands in units of the hopping parameter t.

2.2   Retrieve the Dirac Structure

The band structure of the kagomé lattice, represented in Fig.(2.2), presents some remarkable similarities with the one of graphene. In particular the two non flat bands exhibit Weyl nodes: a discrete set of momentum values where the bands intersect each other and the energy becomes linear in momentum, resembling the dispersion of massless relativistic particles. For this reason they are usually referred to as Dirac points. In fact, the effective Hamiltonian describing the system near these special points turns out to have the two-dimensional Dirac form, as in the graphene case.
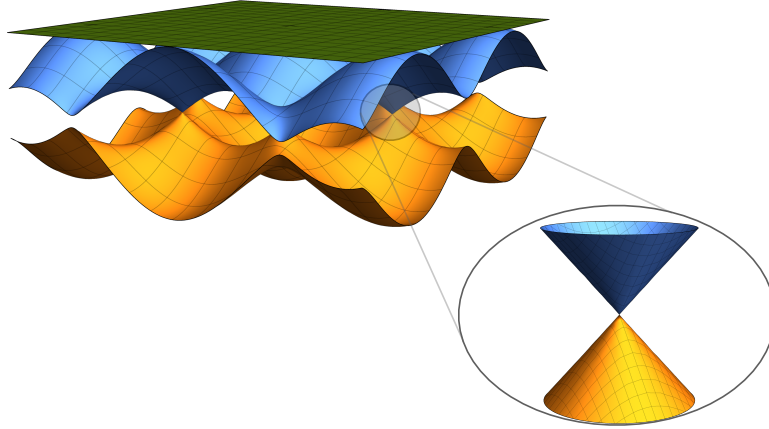
Figure 2.3: Dirac structure in the kagomé spectrum.

Within the first Brillouin zone there are six of these nodes, which again incidentally coincide with the corners of the hexagonal primitive cell in the reciprocal lattice. The boundary conditions impose the equivalence between some of them, such that there are only two in-equivalent Dirac points.
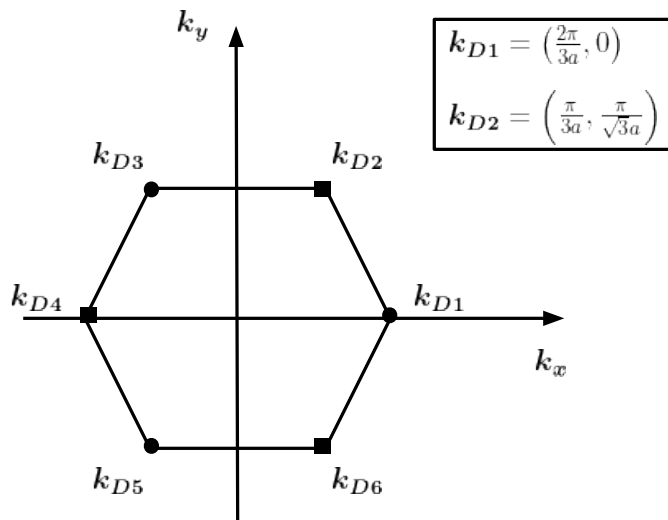
Figure 2.4: First Brillouin zone of the kagomé lattice. The Dirac points sit on its corners. Equivalent points are marked with the same symbol (circle or square).

The purpose of this section is to construct the effective theory, in the vicinity of the Dirac points, for the kagomé lattice. As we will see, the procedure is slightly more complicated than the one for graphene, where expanding the Hamiltonian around the Dirac points was sufficient. This is due to the presence of the additional flat band in the kagomé spectrum, which needs to be decoupled from the other two in order to retrieve the Dirac structure.

Let us start by expanding the one-particle Hamiltonian in eq.(2.9) around $\mathbf{k}_{D1} = (\frac{2\pi}{3a}, 0)$. This is obtained by changing the variables as $\mathbf{k} = \mathbf{k}_{D1} + \mathbf{q}$ and consequently Taylor expand up to linear order in $\mathbf{q}$, assuming $\frac{|\mathbf{q}|}{|\mathbf{k}_{D1}|} \ll 1$.

$$H(\mathbf{k}_{D1}+\mathbf{q}) \simeq t \begin{pmatrix} 0 & 1 + \sqrt{3}aq_x & -1 + \frac{\sqrt{3}}{2}(aq_x + \sqrt{3}aq_y) \\ 1 + \sqrt{3}aq_x & 0 & -1 + \frac{\sqrt{3}}{2}(aq_x - \sqrt{3}aq_y) \\ -1 + \frac{\sqrt{3}}{2}(aq_x + \sqrt{3}aq_y) & -1 + \frac{\sqrt{3}}{2}(aq_x - \sqrt{3}aq_y) & 0 \end{pmatrix}$$

$$(2.11)$$

To make the notation more convenient, in the following we will indicate the Hamiltonian expanded around $\mathbf{k}_{D1}$ as $H_1(\mathbf{q})$.

The goal now is to extract from eq.(2.11) an effective 2×2 Hamiltonian, describing exclusively the two non flat bands near the Dirac point. In other words, the spectrum of the effective Hamiltonian should reproduce correctly, up to linear order in momentum, the dispersion of the two non flat bands in the proximity of $\mathbf{k}_{D1}$.

To achieve this we first evaluate H_1 at $\mathbf{q} = 0$, and find a transformation which diagonalizes the resulting matrix [5]. This is given by

$$U_1 = \begin{pmatrix} \frac{1}{\sqrt{2}} & -\frac{1}{\sqrt{6}} & -\frac{1}{\sqrt{3}} \\ 0 & \sqrt{\frac{2}{3}} & -\frac{1}{\sqrt{3}} \\ \frac{1}{\sqrt{2}} & \frac{1}{\sqrt{6}} & \frac{1}{\sqrt{3}} \end{pmatrix} \qquad (2.12)$$

such that

$$U_1^{-1} H_1(\mathbf{0}) U_1 = \begin{pmatrix} -t & 0 & 0 \\ 0 & -t & 0 \\ 0 & 0 & 2t \end{pmatrix}. \qquad (2.13)$$

Applying the same transformation to $H_1(\mathbf{q})$ (for $\mathbf{q} \neq 0$), we get

$$U_1^{-1} H_1(\mathbf{q}) U_1 = \begin{pmatrix} -t + \frac{1}{2}at\left(\sqrt{3}q_x + 3q_y\right) & \frac{1}{2}at\left(-\sqrt{3}q_y + 3q_x\right) & \frac{1}{2}\sqrt{\frac{3}{2}}at\left(-\sqrt{3}q_x + q_y\right) \\ \frac{1}{2}at\left(-\sqrt{3}q_y + 3q_x\right) & -\frac{1}{2}t\left(\sqrt{3}aq_x + 3aq_y + 2\right) & -\frac{1}{2}\sqrt{\frac{3}{2}}at\left(q_x + \sqrt{3}q_y\right) \\ \frac{at\left(-3q_x + \sqrt{3}q_y\right)}{2\sqrt{2}} & -\frac{1}{2}\sqrt{\frac{3}{2}}at\left(q_x + \sqrt{3}q_y\right) & 2t \end{pmatrix}.$$

$$(2.14)$$

For a more convenient notation in the following we will indicate $U_1^{-1} H_1(\mathbf{q}) U_1 := h_1(\mathbf{q})$. We note en passant that it is important to preserve the hermitian structure of the Hamiltonian, which is the reason why we choose U_1 unitary.

It reveals to be convenient to also perform the following change of variables

$$\begin{cases} q_1 = \tfrac{1}{2}(q_x + \sqrt{3}q_y) \\ q_2 = \tfrac{1}{2}(\sqrt{3}q_x - qy) \end{cases} \tag{2.15}$$

so that the Hamiltonian finally takes the form

$$h_1(q_1, q_2) = \begin{pmatrix} -t + v_f q_1 & v_f q_2 & -\frac{v_f}{\sqrt{2}}q_2 \\ v_f q_2 & -t - v_f q_1 & -\frac{v_f}{\sqrt{2}}q_1 \\ -\frac{v_f}{\sqrt{2}}q_2 & -\frac{v_f}{\sqrt{2}}q_1 & 2t \end{pmatrix} \tag{2.16}$$

where we have defined the kagomé Fermi velocity $v_f = \sqrt{3}at$.

As we can see in eq.(2.16), the eigenvalue $2t$, corresponding to the flat band, appears on the diagonal. This is expected since U_1 is by construction the transformation that diagonalizes $H_1(\mathbf{q})$ at zero-th order in momentum, such that any constant eigenvalue should already pop up on the diagonal after applying U_1.

Having isolated the eigenvalue corresponding to the flat band, the upper-left 2×2 block constitutes the effective Dirac Hamiltonian we were looking for, describing exclusively the two non-flat bands.

$$h_{1eff}(q_1, q_2) = \begin{pmatrix} -t + v_f q_1 & v_f q_2 \\ v_f q_2 & -t - v_f q_1 \end{pmatrix} = -t \cdot \mathbb{1} + v_f(q_1\sigma_3 + q_2\sigma_1). \tag{2.17}$$

However it still remains to prove that the off-block matrix elements in eq.(2.16) contribute to the energy levels of the upper left 2×2 block by terms of order q^2, which can be neglected in the linear regime [5]. This is done in the next paragraph by means of perturbation theory.

2.2.1   Perturbation Theory

Let us consider as the unperturbed Hamiltonian

$$h_1^0(q_1, q_2) = \begin{pmatrix} -t + v_f q_1 & v_f q_2 & 0 \\ v_f q_2 & -t - v_f q_1 & 0 \\ 0 & 0 & 2t \end{pmatrix} \tag{2.18}$$

and as the perturbation

$$V = \begin{pmatrix} 0 & 0 & -\frac{v_f}{\sqrt{2}}q_2 \\ 0 & 0 & -\frac{v_f}{\sqrt{2}}q_1 \\ -\frac{v_f}{\sqrt{2}}q_2 & -\frac{v_f}{\sqrt{2}}q_1 & 0 \end{pmatrix}. \tag{2.19}$$

$h_1^0(q_1, q_2)$ can be exactly diagonalized by the unitary transformation

$$u = \begin{pmatrix} \frac{(q_1+\sqrt{q_1^2+q_2^2})\sqrt{q_2^2}}{q_2\sqrt{2q_1^2+2q_2^2+2q_1\sqrt{q_1^2+q_2^2}}} & \frac{(q_1-\sqrt{q_1^2+q_2^2})\sqrt{q_2^2}}{q_2\sqrt{2q_1^2+2q_2^2-2q_1\sqrt{q_1^2+q_2^2}}} & 0 \\ \frac{\sqrt{q_2^2}}{\sqrt{2q_1^2+2q_2^2+2q_1\sqrt{q_1^2+q_2^2}}} & \frac{\sqrt{q_2^2}}{\sqrt{2q_1^2+2q_2^2-2q_1\sqrt{q_1^2+q_2^2}}} & 0 \\ 0 & 0 & 1 \end{pmatrix} \tag{2.20}$$

as

$$u^{-1} \cdot h_1^0(q_1, q_2) \cdot u = \begin{pmatrix} -t + v_f\sqrt{q_1^2 + q_2^2} & 0 & 0 \\ 0 & -t - v_f\sqrt{q_1^2 + q_2^2} & 0 \\ 0 & 0 & 2t \end{pmatrix} \tag{2.21}$$

meaning that, besides the flat band, the unperturbed energy levels are:

$$E_1 = -t + v_f\sqrt{q_1^2 + q_2^2} \quad \text{and} \quad E_2 = -t - v_f\sqrt{q_1^2 + q_2^2} \tag{2.22}$$

with corresponding eigenstates $|E_1\rangle$, $|E_2\rangle$. On the other hand the perturbation in this basis becomes

$$u^{-1}\cdot V\cdot u \equiv \tilde{V} = -v_f \begin{pmatrix} 0 & 0 & \frac{\sqrt{q_2^2}(2q_1+\sqrt{q_1^2+q_2^2})}{2\sqrt{q_2^2+q_1^2+q_1\sqrt{q_1^2+q_2^2}}} \\ 0 & 0 & \frac{\sqrt{q_2^2}(2q_1-\sqrt{q_1^2+q_2^2})}{2\sqrt{q_2^2+q_1^2-q_1\sqrt{q_1^2+q_2^2}}} \\ \frac{\sqrt{q_2^2}(2q_1+\sqrt{q_1^2+q_2^2})}{2\sqrt{q_2^2+q_1^2+q_1\sqrt{q_1^2+q_2^2}}} & \frac{\sqrt{q_2^2}(2q_1-\sqrt{q_1^2+q_2^2})}{2\sqrt{q_2^2+q_1^2-q_1\sqrt{q_1^2+q_2^2}}} & 0 \end{pmatrix}. \tag{2.23}$$

We can now calculate the correction on the levels E_1, E_2 due to $\tilde{V}$. The perturbative approach is justified here since we assumed $\mathbf{q}$ to be small in the expansion, so indeed $\tilde{V}$ can be treated as a small perturbation.

The first order correction is zero

$$\delta E_1' = \langle E_1|\tilde{V}|E_1\rangle = \delta E_2' = \langle E_2|\tilde{V}|E_2\rangle = 0. \tag{2.24}$$

Whereas at second order we get

$$\delta E_1'' = \sum_{i\neq|E_1\rangle} \frac{|\langle E_1|\tilde{V}|E_i\rangle|^2}{E_1 - E_i} = \frac{q_1^2}{12t} + \frac{q_2^2}{12t} + \frac{q_1|q_2|}{4t} + O(q^3) \tag{2.25}$$

and

$$\delta E_2'' = \sum_{i\neq|E_2\rangle} \frac{|\langle E_2|\tilde{V}|i\rangle|^2}{E_2 - E_i} = \frac{q_1^2}{12t} + \frac{q_2^2}{12t} - \frac{q_1|q_2|}{4t} + O(q^3) \tag{2.26}$$

as we wanted to prove.

2.2.2   Full Effective Hamiltonian

Before continuing with our discussion of the effective theory, a useful remark has to be made. The one-particle Hamiltonian $H(\mathbf{k})$ derived in eq.(2.9) represents just a single block of the full Hamiltonian in momentum space, which is in fact block diagonal in $\mathbf{k}$.

$$H = \begin{pmatrix} H(\mathbf{k}_1) & & & & \\ & H(\mathbf{k}_2) & & & \\ & & \ddots & & \\ & & & H(\mathbf{k}_{N-1}) & \\ & & & & H(\mathbf{k}_N) \end{pmatrix}. \tag{2.27}$$

This is a direct consequence of the translational invariance of the system, and keeping it in mind will make the construction of the full effective theory appear natural.

Generally speaking, an effective theory is a description of the dynamics of a system, valid only in a particular limit. In our specific case, we started by writing down a tight-binding model on the kagomé lattice, and we now aim to restrict the theory in the regime where the electronic momentum values are in the proximity

of the Dirac points. As already said, in the first Brillouin zone there are two in-equivalent Dirac points. Let us choose $\mathbf{k}_{D1}$ and $\mathbf{k}_{D4}$ as in Fig(2.4). Then, morally, this procedure can be seen as restricting the initial Hilbert space to the states

$$|\mathbf{k}_{D1} + \mathbf{q}\rangle \quad , \quad |\mathbf{k}_{D4} + \mathbf{q}\rangle \quad \text{with} \quad \mathbf{q} \sim 0 \tag{2.28}$$

and thus selecting in (2.27) only the diagonal blocks with corresponding momentum values. All the needed information is therefore encoded in the Hamiltonian

$$H_{14}(\mathbf{q}) = \begin{pmatrix} H(\mathbf{k}_{D1} + \mathbf{q}) & 0 \\ 0 & H(\mathbf{k}_{D4} + \mathbf{q}) \end{pmatrix} \tag{2.29}$$

which can be then linearized in $\mathbf{q}$. At that point, if we decouple the flat band and ignore the corresponding rows and columns, the Dirac form of the Hamiltonian becomes apparent.

In the previous paragraphs this procedure has been carried out only for the upper block, corresponding to $H(\mathbf{k}_{D1} + q)$. The same steps can be similarly repeated also for the Hamiltonian expanded around $\mathbf{k}_{D4}$, leading to the final result

$$H_{eff}(q_1, q_2) = \begin{pmatrix} -t + v_f q_1 & -v_f q_2 & 0 & 0 \\ -v_f q_2 & -t - v_f q_1 & 0 & 0 \\ 0 & 0 & -t - v_f q_1 & v_f q_2 \\ 0 & 0 & v_f q_2 & -t + v_f q_1 \end{pmatrix}. \tag{2.30}$$

This can be conveniently written using tensor products of Pauli matrices as

$$H_{eff} = -t(\sigma_0 \otimes \tau_0) + [\sigma_3 \otimes (v_f q_1 \tau_3)] + [\sigma_3 \otimes (v_f q_2 \tau_1)]. \tag{2.31}$$

If we set the chemical potential properly such that the Fermi level lies between the two non flat bands, the first constant term in (2.31) can be neglected and the effective Hamiltonian describing low energy excitations is

$$H_{eff} = v_f[\sigma_3 \otimes (\tau_3 q_1 + \tau_1 q_2)]. \tag{2.32}$$

Up to this point we have omitted for convenience the presence of the spin degree of freedom. Introducing it back, the spin-full effective theory is described by

$$H_{eff} = v_f[s_0 \otimes \sigma_3 \otimes (\tau_3 q_1 + \tau_1 q_2)] \tag{2.33}$$

where again s, σ, τ are Pauli matrices. The first two act as usual on the spin and valley degree of freedom. However for τ we need to be careful. In fact the effective Hamiltonian (2.33) has been obtained after performing a transformation to decouple the flat band and ignoring the corresponding rows and columns. Therefore the sublattice degree of freedom, still present in $H_{14}(\mathbf{q})$, is not intact anymore in H_{eff}. In particular the Pauli matrices τ in (2.33) act on the space of 2-component spinors, whose components contain a combination of the three sublattices.

2.2.3 Hilbert Spaces of the Model

We conclude the treatment of the effective theory with a comment on the different Hilbert spaces that play a role in the description of our model. It will be in fact useful to distinguish them in the following.

We begin by indicating with $\mathcal{H}$ the Hilbert space of the original tight-binding theory. In a sense this is the large landscape that contains all the other Hilbert spaces that we are going to define.

As a first step to build the effective theory, we have then restricted $\mathcal{H}$ to a subset only containing the states (2.28). We call this new Hilbert space $\tilde{\mathcal{H}}$, in which the Hamiltonian $H_{14}(\mathbf{q})$ in (2.29) is expressed before the decoupling procedure of the flat band. The block structure of $H_{14}(\mathbf{q})$ suggests that $\tilde{\mathcal{H}}$ can be broken down into sectors corresponding to the degrees of freedom of the system:

$$\tilde{\mathcal{H}} = \text{spin} \otimes \text{valley} \otimes \text{sublattice}, \tag{2.34}$$

The wave function in $\tilde{\mathcal{H}}$ is therefore a spinor with components

$$\Psi = \begin{pmatrix} \psi_{+,\uparrow}^{A,B,C}, & \psi_{-,\uparrow}^{A,B,C}, & \psi_{+,\downarrow}^{A,B,C}, & \psi_{-,\downarrow}^{A,B,C} \end{pmatrix}^T \quad \text{with} \quad \psi^{A,B,C} = \begin{pmatrix} A & B & C \end{pmatrix}^T. \tag{2.35}$$

Finally, we transformed $H_{14}(\mathbf{q})$ (and accordingly $\tilde{\mathcal{H}}$) by decoupling the flat band, and ignoring the corresponding rows and columns. In this space the Hamiltonian takes the two-dimensional Dirac form. For this reason, we refer to the resulting Hilbert space as the Dirac subspace $\mathcal{H}_D$.

2.2.4 Choice of the Dirac Points

The form of the effective Hamiltonian (2.33) has been derived for a particular choice of in-equivalent Dirac points, namely k_{D1} and k_{D4}. However this choice was completely arbitrary, and we may ask if a different one would have yield the same result. As already said, in the first Brillouin zone there are six Dirac points, corresponding to the corners of its hexagonal edge. The boundary conditions on the hexagon impose that k_{D1} is equivalent to k_{D3}, k_{D5} (and k_{D4} to k_{D2}, k_{D6}). These points are in fact connected by reciprocal lattice vectors. Therefore we would expect our theory to be independent from equivalent valley choice. Things are however more subtle, as we will see it in details later during the discussion of the mass terms, where the Gauge transformations will be introduced. For the time being we simply note that expanding the Hamiltonian around different (although equivalent) Dirac points will result in two different matrices. This means that the transformation that decouples the flat band is in general different for each of the possible choices of Dirac points. However, if we construct the transformations carefully, we are able to obtain the same final effective Dirac Hamiltonian (2.33).

In particular the correct transformations are

$$U_1 = \begin{pmatrix} \frac{1}{\sqrt{2}} & -\frac{1}{\sqrt{6}} & -\frac{1}{\sqrt{3}} \\ 0 & \sqrt{\frac{2}{3}} & -\frac{1}{\sqrt{3}} \\ \frac{1}{\sqrt{2}} & \frac{1}{\sqrt{6}} & \frac{1}{\sqrt{3}} \end{pmatrix} \qquad U_2 = \begin{pmatrix} -\frac{1}{\sqrt{2}} & \frac{1}{\sqrt{6}} & \frac{1}{\sqrt{3}} \\ 0 & \sqrt{\frac{2}{3}} & -\frac{1}{\sqrt{3}} \\ \frac{1}{\sqrt{2}} & \frac{1}{\sqrt{6}} & \frac{1}{\sqrt{3}} \end{pmatrix} \qquad U_3 = \begin{pmatrix} \frac{1}{\sqrt{2}} & -\frac{1}{\sqrt{6}} & -\frac{1}{\sqrt{3}} \\ 0 & -\sqrt{\frac{2}{3}} & \frac{1}{\sqrt{3}} \\ \frac{1}{\sqrt{2}} & \frac{1}{\sqrt{6}} & \frac{1}{\sqrt{3}} \end{pmatrix}$$

$$U_4 = \begin{pmatrix} \frac{1}{\sqrt{2}} & -\frac{1}{\sqrt{6}} & -\frac{1}{\sqrt{3}} \\ 0 & \sqrt{\frac{2}{3}} & -\frac{1}{\sqrt{3}} \\ \frac{1}{\sqrt{2}} & \frac{1}{\sqrt{6}} & \frac{1}{\sqrt{3}} \end{pmatrix} \qquad U_5 = \begin{pmatrix} -\frac{1}{\sqrt{2}} & \frac{1}{\sqrt{6}} & \frac{1}{\sqrt{3}} \\ 0 & \sqrt{\frac{2}{3}} & -\frac{1}{\sqrt{3}} \\ \frac{1}{\sqrt{2}} & \frac{1}{\sqrt{6}} & \frac{1}{\sqrt{3}} \end{pmatrix} \qquad U_6 = \begin{pmatrix} -\frac{1}{\sqrt{2}} & \frac{1}{\sqrt{6}} & -\frac{1}{\sqrt{3}} \\ 0 & \sqrt{\frac{2}{3}} & \frac{1}{\sqrt{3}} \\ -\frac{1}{\sqrt{2}} & -\frac{1}{\sqrt{6}} & \frac{1}{\sqrt{3}} \end{pmatrix}$$

$$\tag{2.36}$$

where U_i works for the Hamiltonian expanded around k_{Di}.

2.3 Opening a Gap

In the previous section we have seen that the band structure of the kagomé lattice is characterized, in the first Brillouin zone, by two in-equivalent Dirac points at the Fermi level. An excitation around these points is linear in momentum, therefore the low energy theory is well described by a two-dimensional massless Dirac Hamiltonian. This emergent relativistic behaviour is a remarkable property that kagomé shares with graphene.

At this point, a natural question that arises is what kind of mass terms can be introduced in the theory, such that the dispersion acquires a gap. This question is relevant in the context of controlling the conduction properties of the material, and has already been address in the graphene case [2]. We now extend the discussion also to kagomé.

We begin by first defining what we mean by mass. Let us consider a generic Dirac Hamiltonian in two dimensions

$$H_D = \alpha_1 k_1 + \alpha_2 k_2, \tag{2.37}$$

where $\alpha_{1,2}$ are two generic anti-commuting objects satisfying

$$\{\alpha_i, \alpha_j\} = 2\delta_{i,j} \quad i,j = 1,2 \quad . \tag{2.38}$$

The Hamiltonian (2.37) simply leads to the gap-less dispersion

$$E = \pm|\mathbf{k}|. \tag{2.39}$$

Let us now add to (2.37) a term of the form mM, where M is an operator and m a constant [2]. Squaring the resulting Hamiltonian yields

$$H_D^2 = k_1^2 + k_2^2 + m^2 M^2 + mk_1\{M, \alpha_1\}mk_2\{M, \alpha_2\} \tag{2.40}$$

where eq.(2.38) has been used. If we require that

$$\{M, \alpha_{1,2}\} = 0 \quad , \quad M^2 = \mathbb{1} \tag{2.41}$$

the resulting dispersion becomes massive

$$E = \pm\sqrt{|\mathbf{k}|^2 + m^2}. \tag{2.42}$$
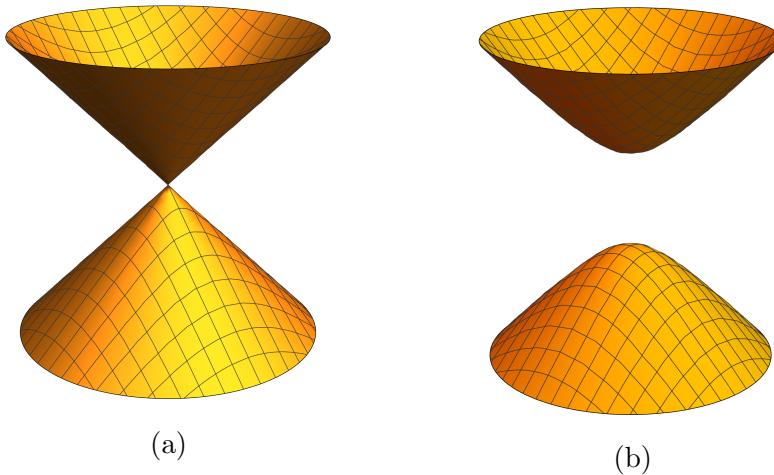

(a)   (b)

Figure 2.5: On the left a massless Dirac dispersion. On the right is the dispersion after introducing a mass term.

A mass term is therefore defined by the relations (2.41). In the kagomé case the Dirac Hamiltonian reads

$$H_D = v_f[s_0 \otimes \sigma_3 \otimes (\tau_3 q_1 + \tau_1 q_2)] \tag{2.43}$$

and we can make the identifications

$$\alpha_1 = s_0 \otimes \sigma_3 \otimes \tau_3 \quad , \quad \alpha_2 = s_0 \otimes \sigma_3 \otimes \tau_1. \tag{2.44}$$

In order to find all the possible mass terms it is convenient to use as basis a tensor product of three Pauli Matrices (plus the identity) $M_{ijk} = s_i \otimes \sigma_j \otimes \tau_k$. In total there are 64 possibilities, among which only 16 [1] satisfy the condition (2.41):

$m_1 = 002$	$m_5 = 102$	$m_9 = 202$	$m_{13} = 302$
$m_2 = 010$	$m_6 = 110$	$m_{10} = 210$	$m_{14} = 310$
$m_3 = 020$	$m_7 = 120$	$m_{11} = 220$	$m_{15} = 320$
$m_4 = 032$	$m_8 = 132$	$m_{12} = 232$	$m_{16} = 332$

Table 2.1: Tensor indices of the kagomé mass terms.

It is important to note that in the derivation of these mass terms we have assumed that momentum is still a good quantum number, meaning that the terms in the list preserve translation invariance. However, in general, it is possible to find other elements that open a gap, obtained by coupling states with different momenta.

Finally, we stress the fact that the form of the mass terms in $\tilde{\mathcal{H}}_D$ is the same for any valley choice. This is because, as already said, the flat band decoupling transformations have been constructed to get the same Dirac Hamiltonian regardless of the Dirac points chosen.

---

[1]16 is also the number of mass terms in the graphene case [2].

2.4   Symmetries

In this section we present the symmetries of the kagomé system. We are going to divide them into two classes: lattice symmetries, and general quantum mechanical symmetries ($\mathcal{T}$, $\mathcal{S}$, $\mathcal{C}$). First we write down the representation of each symmetry operator and the transformation law of the gap-less Hamiltonian under it. We then classify the mass terms depending if they preserve or break the transformation laws. Based on the particular symmetry, we will represent its corresponding operator in a different Hilbert space. In particular, in the case of the lattice symmetries the natural choice is $\tilde{\mathcal{H}}$, since in that space the sublattice degree of freedom is still intact and it is immediate to see how the three sublattices are transformed by reflections and rotations. In the case of time reversal we can either choose $\tilde{\mathcal{H}}$ or $\mathcal{H}_D$, whereas for the remaining quantum symmetries ($\mathcal{C}$, $\mathcal{S}$) the choice is forced to H_D since in the kagomé case those symmetries are exclusively present in the effective Dirac theory.

2.4.1   Time Reversal

As we have already seen, $\tilde{\mathcal{H}}$ can be broken down into three distinct sectors, corresponding to the spin, valley and sublattice degree of freedom. It is therefore sufficient to first find the correct representation of the symmetry operator on each single sector, and then combine them using the tensor product to obtain the full representation.

Let us start by considering the representation of $\mathcal{T}$ on the Hilbert space of spin $\frac{1}{2}$. This is given by

$$\mathcal{T}_{spin\frac{1}{2}} = is_2\mathcal{K} \tag{2.45}$$

where as usual s indicates Pauli matrices and $\mathcal{K}$ indicates complex conjugation [17]. It can be readily verified that it is indeed the correct form by checking that

$$\mathcal{T}s_1\mathcal{T}^{-1} = -s_1 \quad , \quad \mathcal{T}s_2\mathcal{T}^{-1} = -s_2 \quad , \quad \mathcal{T}s_3\mathcal{T}^{-1} = -s_3 \tag{2.46}$$

as expected. To see how the valleys transform, it is sufficient to note that

$$\mathcal{T}|\mathbf{k}\rangle = |-\mathbf{k}\rangle. \tag{2.47}$$

meaning that if we choose opposite Dirac points, these are swapped. Hence the valley degree of freedom transforms with

$$\mathcal{T}_{valley} = \sigma_1. \tag{2.48}$$

The sublattice degree of freedom is left untouched by this transformation. It follows that the full transformation is represented by

$$\mathcal{T} = is_2\mathcal{K} \otimes \sigma_1 \otimes \mathbb{1}_{3x3}. \tag{2.49}$$

With the explicit form of the operator $\mathcal{T}$ at hand, we can verify that the system presents this symmetry by checking eq.(1.50). Indeed the condition holds true, as can be verified choosing for example $H_{14}(\mathbf{k})$.

2.4.2   Sublattice Symmetry

This transformation also goes by the name of Chiral symmetry. It is defined in second quantization as

$$\mathcal{S}\hat{\Psi}_A\mathcal{S}^{-1} = \sum_B (U_S)_{AB}\Psi_B \quad , \quad \mathcal{S}\hat{\Psi}_A^\dagger\mathcal{S}^{-1} = \sum_B \Psi_B^\dagger (U_S^*)_{BA} \tag{2.50}$$

with $U_{\mathcal{S}}$ a unitary matrix [3]. The second quantized Hamiltonian is invariant under $\mathcal{S}$ if

$$\mathcal{S}\mathbf{H}\mathcal{S}^{-1} = \mathbf{H}, \tag{2.51}$$

form which it follows that the one-particle Hamiltonian has to satisfy

$$U_{\mathcal{S}}HU_{\mathcal{S}}^{\dagger} = -H$$
$$U_{\mathcal{S}}H(\mathbf{k})U_{\mathcal{S}}^{\dagger} = -H(\mathbf{k}). \tag{2.52}$$

In order to find the representation of $\mathcal{S}$ it is instructive to first discuss it in the simpler case of graphene, using first quantization language. Ignoring temporarily spin and valleys, a single momentum block of the tight-binding Hamiltonian has the form

$$H(\mathbf{k}) = \begin{pmatrix} 0 & H_{AB} \\ H_{BA}^{\dagger} & 0 \end{pmatrix}, \tag{2.53}$$

where A and B indicate the two different orbitals. As the name suggests, this symmetry acts on the sublattice degree of freedom, flipping the sign of one sublattice with respect to the other. We say that the symmetry is intact if

$$\tau_3 H(\mathbf{k})\tau_3 = -H(\mathbf{k}). \tag{2.54}$$

From this it immediately follows that if $\psi = \begin{pmatrix} \psi_A & \psi_B \end{pmatrix}$ is an eigenstate with energy E, then there exists another eigenstate $\psi = \begin{pmatrix} \psi_A & -\psi_B \end{pmatrix}$ with opposite energy $-E$. Therefore the spectrum is symmetric. In the full low energy theory, with Hamiltonian

$$H(\mathbf{k})_{eff/graphene} = v_f(s_0 \otimes \sigma_0 \otimes \tau_1 k_x + s_0 \otimes \sigma_3 \otimes \tau_2 k_y) \tag{2.55}$$

the basis spinor is

$$\psi = \begin{pmatrix} A_{+\uparrow}, & B_{+\uparrow}, & A_{-\uparrow}, & B_{-\uparrow}, & A_{+\downarrow}, & B_{+\downarrow}, & A_{-\downarrow}, & B_{-\downarrow} \end{pmatrix}, \tag{2.56}$$

therefore the action of the sublattice symmetry operator is

$$\mathcal{S}_{graphene} = s_0 \otimes \sigma_0 \otimes \tau_3. \tag{2.57}$$

The Kagomé lattice does not present this property apparently, because of the presence of the flat band, which spoils the symmetry of the energy spectrum. However it becomes a symmetry if we restrict to the decoupled space $\tilde{\mathcal{H}}_D$, describing exclusively the two non flat bands. Even though the symmetry does not have the same intuitive action as in graphene, we can still write a unitary matrix that anticommutes with the kagomé low energy Hamiltonian

$$H(\mathbf{k})_{eff/kagome} = v_f[s_0 \otimes \sigma_3 \otimes (\tau_3 k_1 + \tau_1 k_2)]. \tag{2.58}$$

In that case the operator is represented as

$$\mathcal{S}_{kagome} = s_0 \otimes \sigma_3 \otimes \tau_2 \tag{2.59}$$

and it can be checked that the kagomé effective low energy Hamiltonian $H(\mathbf{k})_{eff}$ transforms as

$$\mathcal{S}_{kagome} H(\mathbf{k})_{eff} \mathcal{S}_{kagome}^{-1} = -H(\mathbf{k})_{eff}. \tag{2.60}$$

2.4.3 Charge Symmetry

This symmetry is also called particle-hole, as its action is to swap creation and annihilation operators. It is therefore natural to present it in second quantization. $\hat{\mathcal{C}}$ acts on the Fock space as

$$\mathcal{C}\Psi_A\mathcal{C}^{-1} := \sum_B (U_\mathcal{C})^*_{AB}\Psi_B^\dagger \quad , \quad \mathcal{C}\Psi_A^\dagger\mathcal{C}^{-1} := \sum_B (U_\mathcal{C})_{BA}\Psi_B \quad , \quad \mathcal{C}i\mathcal{C}^{-1} = -i \quad (2.61)$$

where $U_\mathcal{C}$ is a unitary matrix [3]. By definition, we say that the system has this symmetry if

$$\mathcal{C}\mathbf{H}\mathcal{C}^{-1} = \mathbf{H}. \tag{2.62}$$

Similarly as for time reversal, we can use eq.(2.62) to find the corresponding symmetry condition for the one-particle Hamiltonian, which reads

$$U_\mathcal{C}^\dagger H^* U = -H, \tag{2.63}$$

and in momentum space becomes

$$\mathcal{C}H(\mathbf{k})\mathcal{C}^{-1} = -H(-\mathbf{k}). \tag{2.64}$$

As we mentioned in the introduction of unitary and anti-unitary transformations, the symmetry condition is always that the operator commutes with the second quantazied Hamiltonian. However this may not be the case for the one-particle Hamiltonian, as happens here.

In order to derive the representation of $\mathcal{C}$, we remind that the sublattice symmetry can be defined as a composition of charge and time reversal

$$\mathcal{S} = \mathcal{T} \cdot \mathcal{C}. \tag{2.65}$$

Therefore inverting the previous relation, and using the representations of $\mathcal{T}$ and $\mathcal{S}$ already derived, we find that

$$\mathcal{S} = s_2 \otimes \sigma_2 \otimes \tau_2 \cdot \mathcal{K}. \tag{2.66}$$

Again it can be verified that (2.64) holds for the kagomé low energy effective Hamiltonian $H_{eff}(\mathbf{k})$.

2.4.4 Lattice Symmetries

We now turn our attention to the geometrical symmetries of the kagomé lattice. These are reflections and rotations that preserve the structure of the lattice. As in the previous section, we will explicitly write down their representations, and verify that the gapless Hamiltonian is symmetric under them. Before doing that, it is useful to review how the spin and valley degree of freedom are affected by these transformations.

2.4.4.1 Transformation of the spin degree of freedom

Let us first recall that on the Hilbert space of spin $\frac{1}{2}$, a rotation of angle θ around the axis $\hat{\boldsymbol{n}}$, is represented by the operator

$$R_{\vec{n}}(\theta) = exp(-i\frac{\theta}{2}\boldsymbol{s} \cdot \hat{\boldsymbol{n}}) = \cos(\frac{\theta}{2}) \cdot \mathbb{1}_{2x2} - i\boldsymbol{s} \cdot \hat{\boldsymbol{n}} \sin(\frac{\theta}{2}), \qquad (2.67)$$

where $\boldsymbol{s} = (s_1, s_2, s_3)$ is the vector of Pauli matrices [17].

On the other hand, reflections require some extra care. A two dimensional reflection with respect to a certain axis $\hat{\boldsymbol{n}}$ crossing the origin can be decomposed into an inversion of all coordinates (parity transformation), followed by a rotation of π around the direction perpendicular to $\hat{\boldsymbol{n}}$, as in Fig.(2.6).

$$\vec{v_P} \to -\vec{v_P} \qquad\qquad\qquad -\vec{v_P} \to R_{\hat{\boldsymbol{n}}}(\pi) \cdot (-\vec{v_P})$$
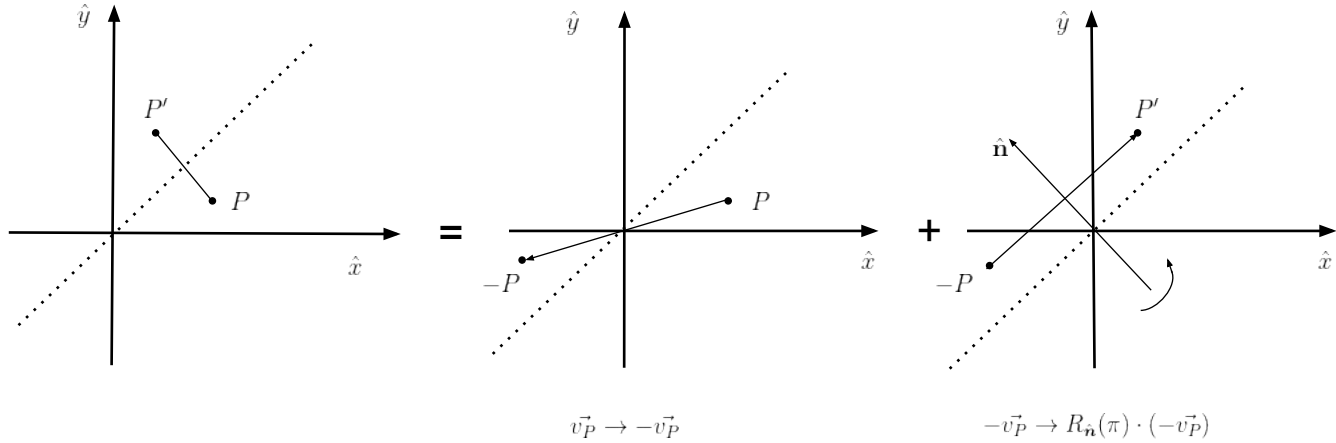
Figure 2.6: Decomposition of a 2D reflection (with respect to an axis crossing the origin) as an inversion of the coordinates followed by a rotation of π around the direction $\hat{n}$, perpendicular to the reflection axis.

This observation turns out to be useful. In fact parity doesn't affect spin, so that only the rotation component needs to be taken into account. The operator representing the reflection is therefore

$$Ref_{\hat{\mathbf{n}}} = -i\boldsymbol{s} \cdot \hat{\boldsymbol{n}}_{\perp} \qquad\qquad (2.68)$$

with $\hat{\boldsymbol{n}}_{\perp}$ the unitary vector perpendicular to the reflection axis.

2.4.4.2 Transformation of the valleys

Reflections and rotations in real space correspond to the same transformations in momentum space. Moreover the reciprocal lattice presents the same symmetries as

the real space structure. Therefore, in order to see how the valleys are affected, we apply the considered transformation to the hexagon representing the first Brillouin zone, and see how the Dirac points at the corners are mapped into each other. As we will see, depending on the particular reflection or rotation, there will be some natural choices for the Dirac points of reference, such that the symmetry operator assumes the simplest form.
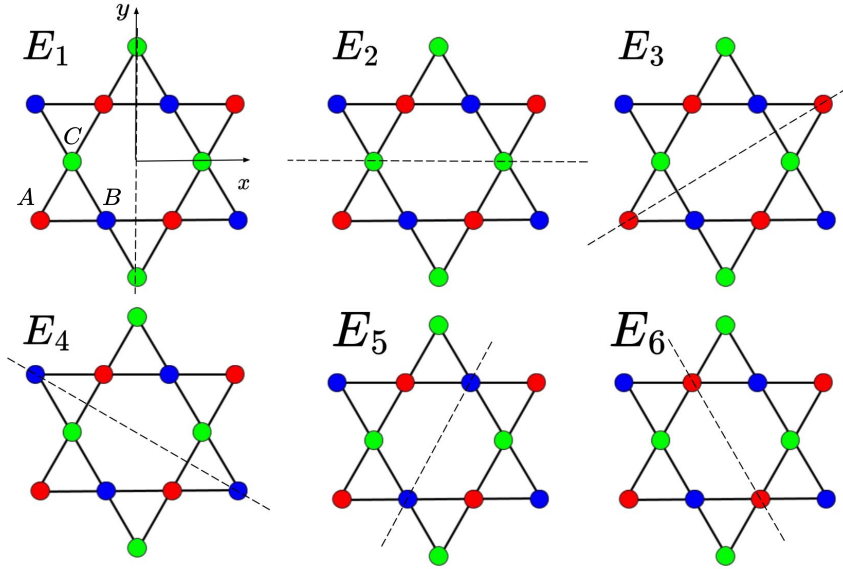
2.4.4.3 Reflections symmetries

Figure 2.7: Reflection symmetries of the kagomé lattice. The dotted lines indicate the axis of reflection. The three sublattices are marked with different colors.

- **E1** : This is the reflection with respect to the $\hat{y}$ axis, and it inverts the k_x momentum component. Using eq.(2.68) the corresponding transformation on the spin sector is

$$E_{1spin} = -i\boldsymbol{s} \cdot \hat{\boldsymbol{x}} = -is_1 \tag{2.69}$$

  where s_1 is the first Pauli matrix.

  Regarding the valleys, a convenient choice for this reflection is to consider Dirac points symmetric with each other with respect to the reflection axis $\hat{y}$, such as k_{D1} and k_{D4}. Given that choice, it is clear that E_1 simply exchanges the two valleys

$$\begin{aligned} \mathbf{k}_{D1} &\to \mathbf{k}_{D4} \\ \mathbf{k}_{D4} &\to \mathbf{k}_{D1}, \end{aligned} \tag{2.70}$$

  meaning that the reflection operator in valley space is represented by

$$E_{1Valley} = \sigma_1. \tag{2.71}$$

  Finally it is immediate to see, by looking at the real space lattice, how the

sublattice degree of freedom transforms:

$$
\begin{aligned}
A &\to B \\
B &\to A \\
C &\to C.
\end{aligned}
\tag{2.72}
$$

Therefore the full transformation is given by

$$
E_1 = -is_1 \otimes \sigma_1 \otimes
\begin{pmatrix}
0 & 1 & 0 \\
1 & 0 & 0 \\
0 & 0 & 1
\end{pmatrix}
\tag{2.73}
$$

Finally, the momentum Hamiltonian expanded around k_{D1} and k_{D4} transforms under the action of E_1 as

$$
E_1 \cdot H_{14}(k_x, k_y) \cdot E_1^{-1} = H_{14}(-k_x, k_y).
\tag{2.74}
$$

- **E2**: This is the reflection with respect to the $\hat{x}$ axis, which inverts the k_y momentum component. The transformation acts on the spin sector as

$$
E_{2spin} = -is_2
\tag{2.75}
$$

A convenient choice for the valleys here is again k_{D1} and k_{D4}, which are left untouched by this reflection. The sublattice degree of freedom changes according to

$$
\begin{aligned}
A &\to B \\
B &\to A \\
C &\to C
\end{aligned}
\tag{2.76}
$$

The full transformation is therefore

$$
E_2 = -is_2 \otimes \sigma_0 \otimes
\begin{pmatrix}
0 & 1 & 0 \\
1 & 0 & 0 \\
0 & 0 & 1
\end{pmatrix}
\tag{2.77}
$$

Finally, the Hamiltonian transforms under the action of E_2 according to

$$
E_2 \cdot H_{14}(k_x, k_y) \cdot E_2^{-1} = H_{14}(k_x, -k_y).
\tag{2.78}
$$

- **E3**: This reflection is with respect to the axis $\hat{n}$ of components

$$
\hat{n} = (\frac{\sqrt{3}}{2}, \frac{1}{2}).
\tag{2.79}
$$

Using some simple trigonometry, the perpendicular direction is

$$
\hat{n}_\perp = (-\frac{1}{2}, \frac{\sqrt{3}}{2}).
\tag{2.80}
$$

It follows that the spin degree of freedom transforms with

$$
E_{3spin} = \frac{i}{2}(s_1 - \sqrt{3}s_2).
\tag{2.81}
$$

Regarding the valleys, a convenient choice is to consider $\mathbf{k}_{D1}$ and $\mathbf{k}_{D2}$, which get swapped by this reflection. Another equivalent possibility is to take $\mathbf{k}_{D4}$ and $\mathbf{k}_{D5}$. The 3 sublattices are reshuffled as:

$$\begin{aligned} A &\to A \\ B &\to C \\ C &\to B \end{aligned} \tag{2.82}$$

The full transformation is therefore

$$E_3 = \frac{i}{2}(s_1 - \sqrt{3}s_2) \otimes \sigma_1 \otimes \begin{pmatrix} 1 & 0 & 0 \\ 0 & 0 & 1 \\ 0 & 1 & 0 \end{pmatrix}. \tag{2.83}$$

Finally, the Hamiltonian expanded around $\mathbf{k}_{D1}, \mathbf{k}_{D2}$ transforms as

$$E_3 \cdot H_{12}(\mathbf{k}) \cdot E_3^{-1} = H_{12}(\boldsymbol{k}') \tag{2.84}$$

where $\boldsymbol{k}'$ is the momentum reflected with respect to $\hat{\boldsymbol{n}}_\perp$

$$\boldsymbol{k}' = (\frac{k_x}{2} + \frac{\sqrt{3}}{2}k_y, \frac{\sqrt{3}}{2}k_x - \frac{k_y}{2}). \tag{2.85}$$

- **E4**: In this case the axis of reflection is

$$\hat{\boldsymbol{n}} = (-\frac{\sqrt{3}}{2}, \frac{1}{2}) \tag{2.86}$$

therefore

$$\hat{\boldsymbol{n}}_\perp = (\frac{1}{2}, \frac{\sqrt{3}}{2}). \tag{2.87}$$

The spin degree of freedom transforms according to

$$E_{4spin} = -\frac{i}{2}(s_1 + \sqrt{3}s_2) \tag{2.88}$$

For the valleys we can conveniently either choose $\mathbf{k}_{D3}$ and $\mathbf{k}_{D4}$ (or $\mathbf{k}_{D1}, \mathbf{k}_{D6}$), which are swapped under E_4. The 3 sublattices are changed as:

$$\begin{aligned} A &\to C \\ B &\to B \\ C &\to A \end{aligned} \tag{2.89}$$

The full transformation is

$$E_4 = -\frac{i}{2}(s_1 + \sqrt{3}s_2) \otimes \sigma_1 \otimes \begin{pmatrix} 0 & 0 & 1 \\ 0 & 1 & 0 \\ 1 & 0 & 0 \end{pmatrix} \tag{2.90}$$

Finally the Hamiltonian transforms as

$$E_4 \cdot H_{34}(\mathbf{k}) \cdot E_4^{-1} = H_{34}(\mathbf{k}') \tag{2.91}$$

where again $\boldsymbol{k}'$ is the reflected momentum under E_4

$$\boldsymbol{k}' = (\frac{k_x}{2} - \frac{\sqrt{3}k_y}{2}, -\frac{\sqrt{3}k_x}{2} - \frac{k_y}{2}). \tag{2.92}$$

- **E5**: For this reflection we have that the axis of reflection and its perpendicular are

$$\hat{\boldsymbol{n}} = (\frac{1}{2}, \frac{\sqrt{3}}{2}) \quad , \quad \hat{\boldsymbol{n}}_\perp = (-\frac{3}{2}, \frac{1}{2}). \tag{2.93}$$

The spin sector transforms under

$$E_{5spin} = \frac{i}{2}(\sqrt{3}s_1 - s_2) \tag{2.94}$$

As for the valleys, we choose $\mathbf{k}_{D5}$ and $\mathbf{k}_{D2}$, which are left untouched by the reflection. The 3 sublattices are shuffled according to

$$\begin{aligned} A &\to C \\ B &\to B \\ C &\to A \end{aligned} \tag{2.95}$$

The full transformation is

$$E_5 = \frac{i}{2}(\sqrt{3}s_1 - s_2) \otimes \sigma_0 \otimes \begin{pmatrix} 0 & 0 & 1 \\ 0 & 1 & 0 \\ 0 & 0 & 1 \end{pmatrix} \tag{2.96}$$

And finally the Hamiltonian transformation law is

$$E_5 \cdot H_{52}(\mathbf{k}) \cdot E_5^{-1} = H_{52}(\mathbf{k}') \tag{2.97}$$

with $\mathbf{k}'$ the momentum reflected with respect to $\hat{\boldsymbol{n}}$

$$\boldsymbol{k}' = (-\frac{k_x}{2} + \frac{\sqrt{3}k_y}{2}, \frac{\sqrt{3}k_x}{2} + \frac{k_y}{2}). \tag{2.98}$$

- **E6**: In this case the reflection axis and its perpendicular are

$$\hat{\boldsymbol{n}} = (-\frac{1}{2}, \frac{\sqrt{3}}{2}) \quad , \quad \hat{\boldsymbol{n}}_\perp = (\frac{\sqrt{3}}{2}, \frac{1}{2}) \tag{2.99}$$

. It follows that the transformation in spin space is

$$E_{6spin} = -\frac{i}{2}(\sqrt{3}s_1 + s_2) \tag{2.100}$$

As for the valleys, the convenient choice here is to take $\mathbf{k}_{D3}$ and $\mathbf{k}_{D6}$, which are left untouched by E_6. The sublattice degree of freedom changes according to

$$\begin{aligned} A &\to A \\ B &\to C \\ C &\to B \end{aligned} \tag{2.101}$$

The full transformation is therefore

$$E_6 = -\frac{i}{2}(\sqrt{3}s_1 + s_2) \otimes \sigma_0 \otimes \begin{pmatrix} 1 & 0 & 0 \\ 0 & 0 & 1 \\ 0 & 1 & 0 \end{pmatrix} \tag{2.102}$$

The action of E_6 on the Hamiltonian is

$$E_6 \cdot H_{36}(\vec{k}) \cdot E_6^{-1} = H_{36}(\vec{k}') \tag{2.103}$$

with $\boldsymbol{k}'$ the reflected momentum with respect to $\hat{\boldsymbol{n}}$

$$\boldsymbol{k}' = (-\frac{k_x}{2} - \frac{\sqrt{3}k_y}{2}, -\frac{\sqrt{3}k_x}{2} + \frac{k_y}{2}). \tag{2.104}$$

2.4.4.4 Rotations

The treatment of rotations follows a similar procedure as for the reflections. However, extra care needs to be paid when writing down the transformation law for the Hamiltonian. In fact, if in the case of reflections we were able to conveniently choose the valleys, such that the transformation could either swap or left them untouched, this is not possible anymore for rotations. In particular, an Hamiltonian expanded around a certain pair of Dirac points will be sent by the rotation in an Hamiltonian corresponding to a different choice of valleys. Therefore, when writing the transformation law, we will need to express it using Hamiltonians expanded around different valleys. The transformation operator on the valley sector will then only keep track of the fact that a Dirac point can either be sent to an equivalent or in-equivalent one by the rotation (this will become clear in the following).
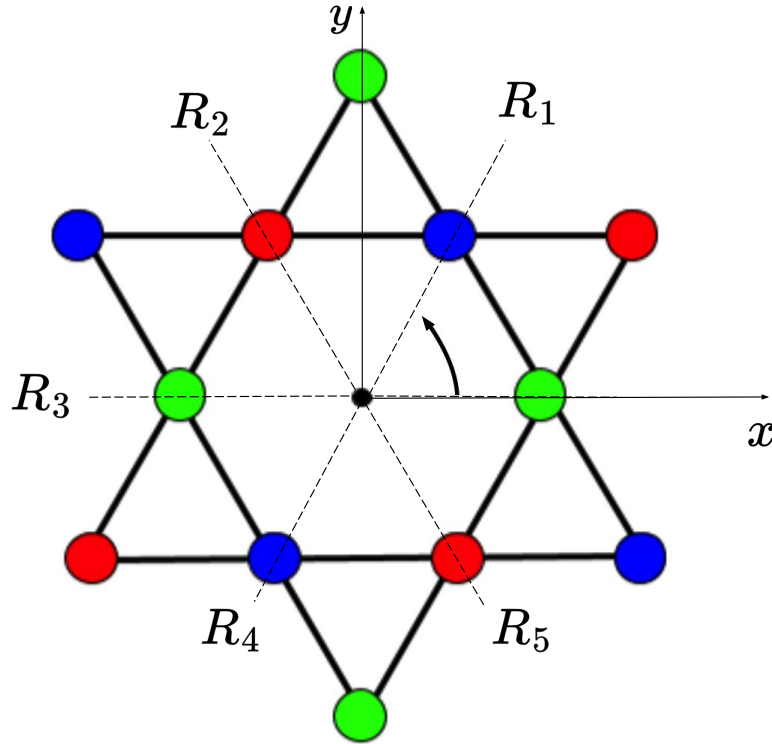

Figure 2.8: Rotation symmetries of kagomé lattice.

- **R1:** This is the rotation of $\theta = \frac{\pi}{3}$, therefore using eq.(2.6) the spin degree of freedom transforms with the operator

$$R_{1spin} = \frac{1}{2}(\sqrt{3}s_0 - is_3). \tag{2.105}$$

As for the valleys, if we choose k_{D1} and k_{D4}, this rotation will send them in

$$\mathbf{k}_{D1} \rightarrow \mathbf{k}_{D2} \quad , \quad \mathbf{k}_{D4} \rightarrow \mathbf{k}_{D5} \tag{2.106}$$

which means that odd valleys are sent into even, and vice versa. This is true for any other choice. Our convention is to always write the Hamiltonian with odd valleys in the upper block and even in the lower. Therefore this rotation acts with a σ_1 in the valley sector, which serves to restore the correct order.

The sublattices are transformed as

$$
\begin{aligned}
A &\to C \\
B &\to A \\
C &\to B
\end{aligned} \tag{2.107}
$$

The full transformation is

$$
R_1 = \frac{1}{2}(\sqrt{3}s_0 - is_3) \otimes \sigma_1 \otimes \begin{pmatrix} 0 & 0 & 1 \\ 1 & 0 & 0 \\ 0 & 1 & 0 \end{pmatrix}. \tag{2.108}
$$

Finally the transformation law for the Hamiltonian reads

$$
R_1 \cdot H_{14}(\mathbf{k}) \cdot R_1^{-1} = H_{54}(\boldsymbol{k}') \tag{2.109}
$$

where here, and in the following, we indicate with $\boldsymbol{k}'$ the rotated of $\boldsymbol{k}$ by the angle of the rotation (in this case $\frac{\pi}{3}$).

- **R2:** This is the rotation of $\frac{2\pi}{3}$. Spin is transformed with

$$
R_{2spin} = \frac{1}{2}(s_0 - i\sqrt{3}s_3). \tag{2.110}
$$

The parity of the Dirac points number is not changed by this transformation, so we have a σ_0 acting in the valley sector. Again it is easy to see how the sub-lattices change

$$
\begin{aligned}
A &\to B \\
B &\to C \\
C &\to A
\end{aligned} \tag{2.111}
$$

The full transformation is

$$
\frac{1}{2}(s_0 - i\sqrt{3}s_3) \otimes \sigma_0 \otimes \begin{pmatrix} 0 & 1 & 0 \\ 0 & 0 & 1 \\ 1 & 0 & 0 \end{pmatrix}, \tag{2.112}
$$

and the Hamiltonian transformation law can be expressed as

$$
R_2 \cdot H_{14}(\mathbf{k}) \cdot R_2^{-1} = H_{36}(\boldsymbol{k}') \tag{2.113}
$$

where again $\boldsymbol{k}'$ is the rotated of $\mathbf{k}$ by $\frac{2\pi}{3}$.

- **R3:** This is the rotation of π. The operator that represents R_3 in spin space is

$$
R_{3spin} = -is_3 \tag{2.114}
$$

Here it is convenient to choose as reference opposite Dirac points, such that the transformation simply swaps them. The lattice is left untouched

$$
\begin{aligned}
A &\to A \\
B &\to B \\
C &\to C
\end{aligned} \tag{2.115}
$$

The full operator is

$$R3 = -is_3 \otimes \sigma_1 \otimes \begin{pmatrix} 1 & 0 & 0 \\ 0 & 1 & 0 \\ 0 & 0 & 1 \end{pmatrix}, \tag{2.116}$$

and the transformation law for the Hamiltonian reads

$$R_3 \cdot H_{14}(\mathbf{k}) \cdot R_3^{-1} = H_{14}(\mathbf{k}') \tag{2.117}$$

with $\mathbf{k}' = (-k_x, -k_y)$.

- **R4:** This is the rotation of $\frac{4\pi}{3}$. For the spin we have

$$R_{4spin} = -\frac{1}{2}(s_0 + i\sqrt{3}s_3) \tag{2.118}$$

A possible choice for the Dirac points is $\mathbf{k}_{D1}$ and $\mathbf{k}_{D4}$, which are sent to

$$\mathbf{k}_{D1} \to \mathbf{k}_{D5} \quad , \quad \mathbf{k}_{D4} \to \mathbf{k}_{D2}. \tag{2.119}$$

Therefore the valley number does not change parity. Sublattices are reshuffled as

$$\begin{aligned} A &\to C \\ B &\to A \\ C &\to B \end{aligned} \tag{2.120}$$

The full operator is

$$R_4 = -\frac{1}{2}(s_0 + i\sqrt{3}s_3) \otimes \sigma_0 \otimes \begin{pmatrix} 0 & 0 & 1 \\ 1 & 0 & 0 \\ 0 & 1 & 0 \end{pmatrix} \tag{2.121}$$

and the transformation law for the Hamiltonian is:

$$R_4 \cdot H_{14}(\mathbf{k}) \cdot R_4^{-1} = H_{52}(\mathbf{k}'). \tag{2.122}$$

where $\mathbf{k}'$ is the rotation of the vector $\mathbf{k} = (k_x, k_y)$ of $\frac{4\pi}{3}$.

- **R5:** This is the rotation of $\frac{5\pi}{3}$ We have

$$R_{5spin} = -\frac{1}{2}(\sqrt{3}s_0 + is_3) \tag{2.123}$$

The valley number changes parity, so a σ_1 acts on that degree of freedom. The sublattices transform as

$$\begin{aligned} A &\to B \\ B &\to C \\ C &\to A \end{aligned} \tag{2.124}$$

The full transformation is

$$-\frac{1}{2}(\sqrt{3}s_0 + is_3) \otimes \sigma_1 \otimes \begin{pmatrix} 0 & 1 & 0 \\ 0 & 0 & 1 \\ 1 & 0 & 0 \end{pmatrix} \tag{2.125}$$

And finally the Hamiltonian transformation law is

$$R_5 \cdot H_{14}(\mathbf{k}) \cdot R_5^{-1} = H_{36}(\mathbf{k}') \tag{2.126}$$

where $\mathbf{k}'$ is the rotation of the vector $\mathbf{k} = (k_x, k_y)$ of $\frac{5\pi}{3}$.

2.4.5 Classification of Mass Terms

In the previous section we have analyzed all the symmetries of the gap-less tight-binding model for the kagomé lattice. On the other hand, as seen in section(2.3), it is possible to introduce a list of instabilities in the model, such that the underlying Dirac theory becomes massive, and the spectrum acquires a gap.

In this section we bring these two pieces together, and see how the previously discussed symmetries are affected by the presence of mass. It is reasonable to expect that, depending on the particular mass term, some symmetries will be preserved and other broken. In particular, we say that a symmetry is left intact if the corresponding transformation law still holds true for the massive Hamiltonian.

Our goal is therefore to classify all the possible mass terms, based on the symmetries they preserve or break. To do that, it is convenient to transform the mass terms from the Dirac subspace, back to the the non-decoupled space $\tilde{\mathcal{H}}$. This is because the majority of the symmetry transformations are naturally expressed in the latter. The procedure is explicitly demonstrated in the following, taking m_1 as guide example.

2.4.5.1 Example: $m_1 = 002$

Suppose we start with the mass term $m_1 = 002$ in the Dirac subspace, and arbitrarily choose $\mathbf{k}_{D1}$ and $\mathbf{k}_{D4}$ as our reference valleys, such that the Hamiltonian in the decoupled space $\tilde{\mathcal{H}}$ is H_{14}. Our goal is then to transform m_1 in the space $\tilde{\mathcal{H}}$ (where H_{14} is expressed). The procedure consists of the following steps:

- we insert back the rows and columns (of zeros), corresponding to the flat band previously ignored. As a result we get a 12×12 matrix as follows

$$m_1 = s_0 \otimes \sigma_0 \otimes \begin{pmatrix} 0 & -i \\ i & 0 \end{pmatrix} \rightarrow s_0 \otimes \sigma_0 \otimes \begin{pmatrix} 0 & -i & 0 \\ i & 0 & 0 \\ 0 & 0 & 0 \end{pmatrix} := \tilde{m}_1 \qquad (2.127)$$

- Then we transform the so obtained object, restoring the coupling of the flat band with the inverse of the proper U as provided in eq.(2.36), depending on the valley choice. In this particular case

$$\left(\begin{array}{cc|cc} U_1 & 0 & & \\ 0 & U_4 & \multicolumn{2}{c}{\mathbf{0}} \\ \hline \multicolumn{2}{c|}{\mathbf{0}} & U_1 & 0 \\ & & 0 & U_4 \end{array} \right) \cdot \tilde{m}_1 \cdot \left(\begin{array}{cc|cc} U_1^{-1} & 0 & & \\ 0 & U_4^{-1} & \multicolumn{2}{c}{\mathbf{0}} \\ \hline \multicolumn{2}{c|}{\mathbf{0}} & U_1^{-1} & 0 \\ & & 0 & U_4^{-1} \end{array} \right) := M_{002}^{14}$$

  where we introduced the notation M_{ijk}^{ab} to indicate the mass term $s_i \otimes \sigma_j \otimes \tau_k$ in the Dirac space, transformed back to the original non decoupled space, with choice of valleys a and b.

  The resulting matrix M_{002}^{14}, if added to the mass-less Hamiltonian H_{14}, will indeed lift the degeneracy at the Dirac points $\mathbf{k}_{D1}$ and $\mathbf{k}_{D4}$, producing a gap. On the other hand, as a consequence of the boundary conditions, the valley corresponding to $\mathbf{k}_{D1}$ is equivalent to $\mathbf{k}_{D3}$ and $\mathbf{k}_{D5}$ (and 4 to 2,6) meaning that, if a mass term produces a gap at two in-equivalent valleys, it should open a gap in all of the others as well. Therefore we would naively expect M_{002}^{14} to be a good mass term also for an Hamiltonian expanded at different valleys. This turns out to not be the case. More concretely, for example $H_{32} + M_{002}^{14}$ remains massless. The reason for this apparent contradiction is subtle, and the next paragraph is devoted to solve this problem.

2.4.5.2   Gauge Transformations

We have previously stated that the six Dirac points in the first Brillouin zone are divided in two groups of three equivalent valleys, as in Fig.(2.4). However this information is not apparent in the form of the Hamiltonian. In fact, if we evaluate $H(\mathbf{k})$ at equivalent Dirac points (for example $\mathbf{k}_{D1}$ and $\mathbf{k}_{D3}$) we end up with two different matrices

$$H(\mathbf{k}_{D1}) = \begin{pmatrix} 0 & -1 & 1 \\ -1 & 0 & 1 \\ 1 & 1 & 0 \end{pmatrix} \quad , \quad H(\mathbf{k}_{D3}) = \begin{pmatrix} 0 & 1 & 1 \\ 1 & 0 & -1 \\ 1 & -1 & 0 \end{pmatrix}. \tag{2.128}$$

We have already mentioned indirectly this problem, when stating the fact that the U transformation that decouples the flat band (constructed as the matrix that diagonalizes at zero-th momentum order the Hamiltonian) is different depending on the Dirac point considered.

    This might be confusing at first glance, since we would expect the Hamiltonian to be same if evaluated at points connected by reciprocal lattice vectors. The information about the boundary conditions is however still encoded in the fact that $H(\mathbf{k}_{D1})$ and $H(\mathbf{k}_{D3})$ show the same spectrum. In fact, what need to be invariant are the observables (in this case the energy), and not necessarily the form of the Hamiltonian. This suggests that there exists a Gauge transformation that connects $H(\mathbf{k}_{D1})$ and $H(\mathbf{k}_{D3})$. In particular it is given by

$$g_{13} = \begin{pmatrix} 1 & 0 & 0 \\ 0 & -1 & 0 \\ 0 & 0 & 1 \end{pmatrix} \tag{2.129}$$

such that

$$g_{13} \cdot H(\mathbf{k}_{D1}) \cdot g_{13}^{-1} = H(\mathbf{k}_{D3}). \tag{2.130}$$

Similarly we can find the Gauge transformations connecting any pair of Hamiltonians evaluated at equivalent Dirac points

$$g_{13} = \begin{pmatrix} 1 & 0 & 0 \\ 0 & -1 & 0 \\ 0 & 0 & 1 \end{pmatrix} \qquad g_{15} = \begin{pmatrix} -1 & 0 & 0 \\ 0 & 1 & 0 \\ 0 & 0 & 1 \end{pmatrix} \tag{2.131}$$

$$g_{24} = \begin{pmatrix} -1 & 0 & 0 \\ 0 & 1 & 0 \\ 0 & 0 & 1 \end{pmatrix} \qquad g_{26} = \begin{pmatrix} 1 & 0 & 0 \\ 0 & 1 & 0 \\ 0 & 0 & -1 \end{pmatrix} \tag{2.132}$$

Any other possibility is obtained by a composition of the previous. For instance

$$g_{35} = g_{15} \cdot g_{13} = \begin{pmatrix} -1 & 0 & 0 \\ 0 & -1 & 0 \\ 0 & 0 & 1 \end{pmatrix} \tag{2.133}$$

    It follows that a mass term M_{ijk}^{ab} for the Hamiltonian H_{ab}, of valleys a and b, would no longer be a mass term for H_{cd} (different valleys), unless we perform the right Gauge transformation on it.

    In the specific case mentioned in the previous paragraph, M_{002}^{14} transformed to the valleys 3,2 becomes

$$
\begin{pmatrix}
\begin{array}{cc|c}
g_{13} & 0 & \\
0 & g_{42} & \mathbf{0} \\
\hline
& & g_{13} \quad 0 \\
\mathbf{0} & & 0 \quad g_{42}
\end{array}
\end{pmatrix}
\cdot M_{002}^{14} \cdot
\begin{pmatrix}
\begin{array}{cc|c}
g_{13}^{-1} & 0 & \\
0 & g_{42}^{-1} & \mathbf{0} \\
\hline
& & g_{13}^{-1} \quad 0 \\
\mathbf{0} & & 0 \quad g_{42}^{-1}
\end{array}
\end{pmatrix}
$$

which opens correctly a gap in the spectrum of H_{32}.

2.4.5.3   Map the mass terms coming from different valleys

At this point we might ask what is the relation between the mass terms transformed from the Dirac representation into the space $\tilde{\mathcal{H}}$ for different valley choices.

$$
M_{ijk}^{ab} \overset{?}{\longleftrightarrow} M_{lmn}^{cd}. \tag{2.134}
$$

In general we would expect that if we gauge transform M_{ijk}^{ab}, the result would be a combination of mass terms in the new valleys. However it turns out that not only M_{ijk}^{ab}, if properly gauged transformed, becomes a mass term for H_{cd}, but it is precisely equal to M_{ijk}^{cd}:

$$
\begin{pmatrix}
\begin{array}{cc|c}
g_{ac} & 0 & \\
0 & g_{bd} & \mathbf{0} \\
\hline
& & g_{ac} \quad 0 \\
\mathbf{0} & & 0 \quad g_{bd}
\end{array}
\end{pmatrix}
\cdot M_{ijk}^{ab} \cdot
\begin{pmatrix}
\begin{array}{cc|c}
g_{ac}^{-1} & 0 & \\
0 & g_{bd}^{-1} & \mathbf{0} \\
\hline
& & g_{ac}^{-1} \quad 0 \\
\mathbf{0} & & 0 \quad g_{bd}^{-1}
\end{array}
\end{pmatrix}
= M_{ijk}^{cd}. \tag{2.135}
$$

Therefore the mapping between mass terms in $\tilde{\mathcal{H}}$ for different the valleys is the simplest possible: the identity. This is true in the particular choice we made of the decoupling transformations in eq.(2.36). For different choices one might get an overall minus sign on the right hand side of eq.(2.135).

This also means that the form of the mass terms in the Dirac subspace will be the same independently of the valley choice. Therefore it makes sense referring to them by their tensorial indices in $\mathcal{H}_D$, which uniquely identify them.

2.4.5.4   Classification table of the kagomé mass terms

Finally we are ready to present the symmetry classification of the kagomé mass terms.[2]

ijk	E1	E2	E3	E4	E5	E6	R1	R2	R3	R4	R5
002	false	false	false	false	false	false	true	true	true	true	true
010	true	true	true	true	true	true	true	true	true	true	true
020	false	true	false	false	true	true	false	true	false	true	false
032	true	false	true	true	false	false	false	true	false	true	false
102	false	true	false	false	false	false	false	false	false	false	false
110	true	false	false	false	false	false	false	false	false	false	false
120	false	false	false	false	false	false	false	false	true	false	false
132	true	true	false	false	false	false	false	false	true	false	false
202	true	false	false	false	false	false	false	false	false	false	false
210	false	true	false	false	false	false	false	false	false	false	false
202	true	false	false	false	false	false	false	false	false	false	false
232	false	false	false	false	false	false	false	false	true	false	false
302	true	true	true	true	true	true	true	true	true	true	true
310	false	false	false	false	false	false	true	true	true	true	true
320	true	false	true	true	false	false	false	true	false	true	false
332	false	true	false	false	true	true	false	true	false	true	false

	$\mathcal{T}$	$\mathcal{C}$	$\mathcal{S}$
002	false	true	false
010	true	true	true
020	true	true	true
032	true	false	false
102	true	false	false
110	false	false	true
120	false	false	true
132	false	true	false
202	true	false	false
210	false	false	true
220	false	false	true
232	false	true	false
302	true	false	false
310	false	false	true
320	false	false	true
332	false	true	false

---

[2]In the classification "true" and "false" correspond respectively to preserved or broken symmetry. The first column of the table contains the tensorial inidces of the mass terms $m_{ijk} = s_i \otimes \sigma_j \otimes \tau_k$.

Chapter 3

Strained Graphene

3.1 General Overview

In this chapter we are going to consider the effects of strain in the case of graphene. Employing a tight-binding description, we analyse the induced changes on the band structure and particularly on the Dirac cones. The possibility to open a gap in the spectrum is explored through different types of strain. Finally we investigate the connection between the strain-induced gap and mass terms within the usual Dirac theory.

3.1.1 Tight-binding Hamiltonian in the Strained Case

We begin by recalling the tight-binding Hamiltonian for graphene with nearest neighbour hopping which, in the unstrained case, reads

$$\mathbf{H} = -t_0 \sum_{<i,j>,\sigma} (a_{i,\sigma}^\dagger b_{j,\sigma} + h.c.). \tag{3.1}$$

As already said, the parameter t_0 encodes the electronic probability amplitude for the hopping between two neighbouring sites to occur and, in the unstrained scenario, it is such that

$$t_{ij} = t_0 = 2.7 \; eV \; , \forall ij \text{ nearest neighbours} \tag{3.2}$$

being a consequence of the constant bond lengths between carbon atoms.

When strain is introduced, the distances between neighbors are modified

$$\boldsymbol{\delta} \to \boldsymbol{\delta}' = (I + \hat{\epsilon})\boldsymbol{\delta} \tag{3.3}$$

with $\hat{\epsilon}$ the strain tensor, for which we are going to provide more details in the following. As a result, we will have in general a different hopping parameter t_{ij} for each neighbouring pairs $\langle i, j \rangle$. In particular we assume that the value of t_{ij} depends on the module of the vector $\boldsymbol{\delta}_{ij}$ connecting the two neighboring sites $\langle i, j \rangle$, and follows an exponential decay law [14],[16],[15], [4]:

$$t(\boldsymbol{\delta}') = t_0 e^{-\beta(\frac{|\boldsymbol{\delta}'|}{a} - 1)} \tag{3.4}$$

with $\beta = 3.37$ and $a = 1.28A$ the unstrained bond length (which in the following is set to 1 for convenience). The Hamiltonian is hence modified as follows

$$\mathbf{H} = -\sum_{\langle i,j \rangle,\sigma} t_{ij}(a_{i,\sigma}^\dagger b_{j,\sigma} + h.c.) \tag{3.5}$$

and can be rewritten conveniently as

$$\mathbf{H} = - \sum_{i \in A, \boldsymbol{\delta}', \sigma} t(\boldsymbol{\delta}')(a_{i,\sigma}^{\dagger} b_{i+\boldsymbol{\delta}',\sigma} + h.c.). \tag{3.6}$$

In what follows, we are going to consider the case where the strain applied preserves the translation symmetry of the system, such that the Hamiltonian maintains the block diagonal form in momentum space. Therefore, performing the Fourier transform and replicating the calculations of the first chapter, we can cast the Hamiltonian as

$$\mathbf{H} = \sum_{k,\sigma} \begin{pmatrix} a_{k,\sigma}^{\dagger} & b_{k,\sigma}^{\dagger} \end{pmatrix} \cdot \begin{pmatrix} 0 & \Delta \\ \Delta^* & 0 \end{pmatrix} \cdot \begin{pmatrix} a_{k,\sigma} \\ b_{k,\sigma} \end{pmatrix}, \tag{3.7}$$

where

$$\Delta := \sum_j t(\boldsymbol{\delta}_j') e^{-i\mathbf{k}\cdot\boldsymbol{\delta}_j'} = \sum_j t((I+\hat{\epsilon})\boldsymbol{\delta}_j) e^{-i\mathbf{k}\cdot(I+\hat{\epsilon})\boldsymbol{\delta}_j}, \tag{3.8}$$

and the matrix

$$H(k) := \begin{pmatrix} 0 & \Delta \\ \Delta^* & 0 \end{pmatrix} \tag{3.9}$$

is the usual Block Hamiltonian. Finally, the energy spectrum is easily obtained by diagonalizing $H(k)$

$$E(k) = \pm \left| \sum_j t(\delta_j') e^{-i\mathbf{k}\cdot\boldsymbol{\delta}_j'} \right|. \tag{3.10}$$

3.1.2   Strain-induced Effects on the Dirac Points

As the numerical results of the next section will confirm, the application of strain can indeed lead to the opening of a gap in the energy spectrum, which occurs concurrently with the merging of in-equivalent Dirac points. In particular in this paragraph we investigate analytically how strain affects their position in momentum space.

By definition, the position of the Dirac points is determined by the condition

$$E(k) = \pm \left| \sum_j t(\boldsymbol{\delta}_j') e^{-i\mathbf{k}\cdot(I+\epsilon)\boldsymbol{\delta}_j} \right| = 0. \tag{3.11}$$

It reveals to be a convenient choice to make the following change of variables in momentum space [15]:

$$\mathbf{k} \to \tilde{\mathbf{k}} = (I + \hat{\epsilon})^T \mathbf{k} \tag{3.12}$$

such that the energy dispersion becomes similar to the unstrained case

$$E(\mathbf{k}) = \pm \left| \sum_j t(\boldsymbol{\delta}_j') e^{-i\tilde{\mathbf{k}}\cdot\boldsymbol{\delta}_j} \right| = 0, \tag{3.13}$$

with the presence of three distinct hopping parameters being the only difference. This procedure is in fact equivalent to only consider the changes produced by the strain on the hopping parameters, while keeping the lattice untouched [15]. The advantage gained is that the reciprocal lattice vectors in $\tilde{\mathbf{k}}$ space will not be modified by strain

$$\mathbf{b}_1 = (\frac{2\pi}{3}; \frac{2\pi\sqrt{3}}{3}) \quad \text{and} \quad \mathbf{b}_2 = (\frac{2\pi}{3}; -\frac{2\pi\sqrt{3}}{3}) \tag{3.14}$$

hence the Brillouin zone is not deformed. In the following we will mark a point with an upper tilde "∼" to indicate that its coordinates are expressed in this particular momentum space.
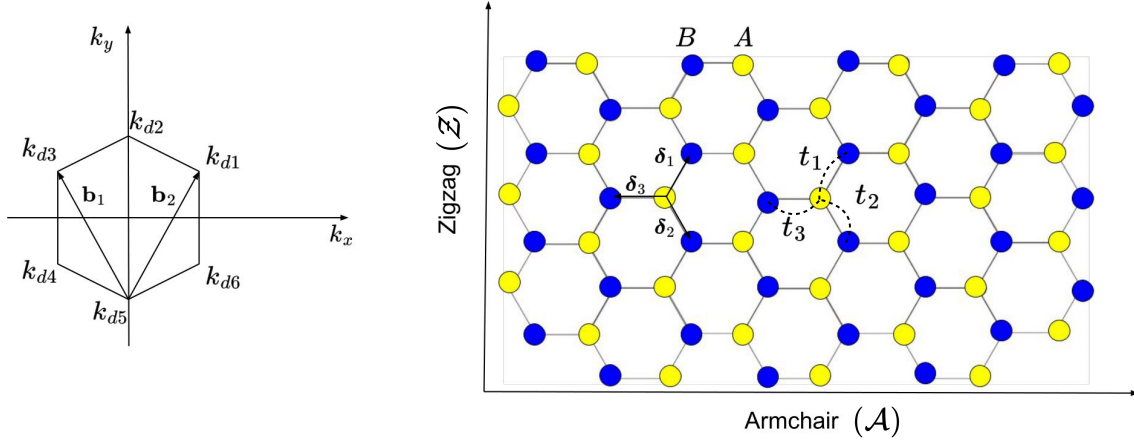

Figure 3.1: Brillouin zone in **k** space and real space lattice representations.

Keeping this in mind, using the expression of the three unstrained bonds $\delta_{1,2,3}$, we can explicitly evaluate the condition (3.11) as

$$t_1^2 + t_2^2 + t_3^2 + 2t_1 t_2 \cos(\sqrt{3}\tilde{k}_y) + 2t_2 t_3 \cos(\frac{3}{2}\tilde{k}_x - \frac{\sqrt{3}}{2}\tilde{k}_y) + 2t_1 t_3 \cos(\frac{3}{2}\tilde{k}_x + \frac{\sqrt{3}}{2}\tilde{k}_y) = 0 \tag{3.15}$$

Let us first find the solution in the special case of uni-axial strain along $\mathcal{Z}$.

- **Zig-Zag uni-axial strain ($\mathcal{Z}$):** In this case $t_1 = t_2 \neq t_3$ and it is easy to guess one possible solution [16]:

$$\tilde{\mathbf{K}} = (0, \pm\frac{2}{\sqrt{3}}\arccos(-\frac{t_3}{2t_1})). \tag{3.16}$$

As a consistency check, we can evaluate it for $t_1 = t_3$, corresponding to null strain, and verify that it correctly reduces to the two in-equivalent Dirac points

$$\mathbf{k}_{d2} = (0, \frac{4\pi}{3\sqrt{3}}) \quad , \quad \mathbf{k}_{d5} = (0, -\frac{4\pi}{3\sqrt{3}}). \tag{3.17}$$

Having found these two particular solutions, all the others can be readily generated by adding reciprocal lattice vectors. In particular, for the two usual in-equivalent Dirac points of our choice, we have

$$\tilde{\mathbf{k}}_{d1} = \frac{2}{\sqrt{3}}(\frac{\pi}{\sqrt{3}}; \pi - \arccos(-\frac{t_3}{2t_1}))$$

$$\tilde{\mathbf{k}}_{d6} = \frac{2}{\sqrt{3}}(\frac{\pi}{\sqrt{3}}; -\pi + \arccos(-\frac{t_3}{2t_1})). \tag{3.18}$$

As anticipated, these points shift as the hopping parameters change, and do not coincide anymore with the corners of the Brillouin zone. It is also apparent from eq.(3.18) that when $2t_1 = t_3$, $\tilde{\mathbf{k}}_{d1}$ and $\tilde{\mathbf{k}}_{d6}$ will merge in

$$\tilde{\boldsymbol{M}}_1 = (\frac{2\pi}{3}; 0). \tag{3.19}$$

After merge has taken place, if the intensity of the strain is further increased, a gap is opened in the spectrum and the condition (3.11) for the Dirac points does not hold anymore. However it is worth noting that the local minimum of the upper energy band E_+ (or equivalently the local maximum of the lower band E_-) will still lie at position $\tilde{\boldsymbol{M}}_1$ (in $\tilde{\mathbf{k}}$ space). In fact the gradient of E_+^2 evaluated at $\tilde{\boldsymbol{M}}_1$ is always zero, whereas the Hessian reads:

$$\begin{pmatrix} \frac{\partial^2 E_+^2}{\partial \tilde{k}x \partial \tilde{k}x} & \frac{\partial^2 E_+^2}{\partial \tilde{k}x \partial \tilde{k}y} \\ \frac{\partial^2 E_+^2}{\partial \tilde{k}y \partial \tilde{k}x} & \frac{\partial^2 E_+^2}{\partial \tilde{k}y \partial \tilde{k}y} \end{pmatrix}_{/\tilde{\boldsymbol{M}}_1} = \begin{pmatrix} 9t_1 t_3 & 0 \\ 0 & 3t_1(t_3 - 2t_1) \end{pmatrix}. \tag{3.20}$$

Considering the sign of its determinant, we see that for $t_3 < 2t_1$ (before merge) $\tilde{\boldsymbol{M}}_1$ is a saddle point. Whereas for $t_3 > 2t_1$ (after merge) $\tilde{\boldsymbol{M}}_1$ becomes a local minimum.

(a) $\epsilon = 0$ (b) $\epsilon = 0.17$

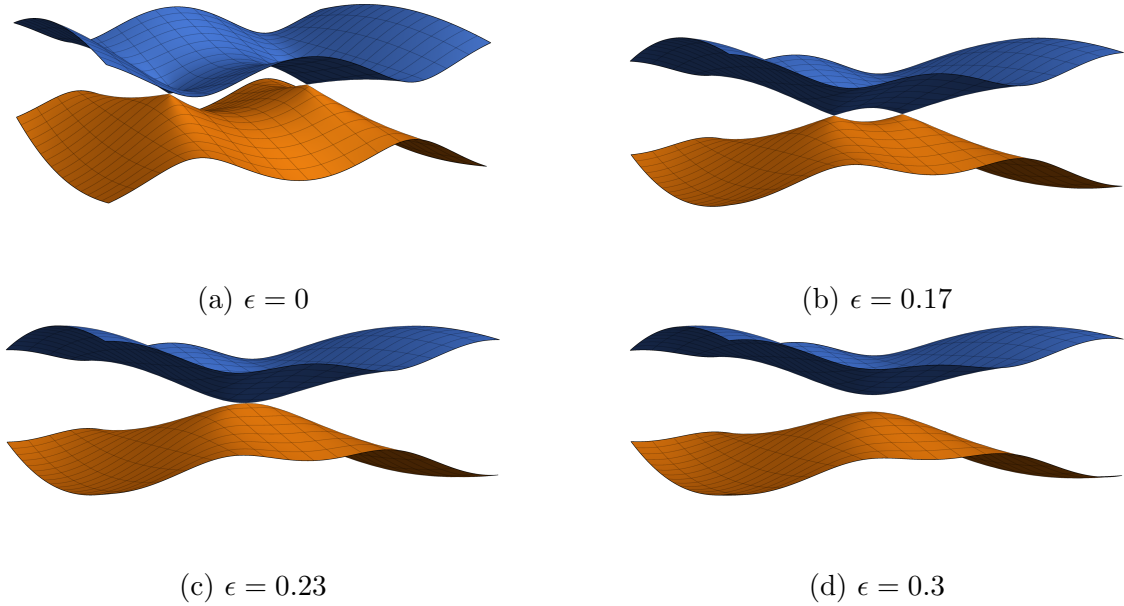(c) $\epsilon = 0.23$ (d) $\epsilon = 0.3$

Figure 3.2: Merging of the Dirac cones for a strain along $\mathcal{Z}$.

- **Generic strain:** In the case where a generic strain is chosen, the merging of in-equivalent Dirac points will still occur, as the numerical analysis will show. Moreover it can be proven generally that the point of merge can only be either the origin, or one of the four $\tilde{\boldsymbol{M}}_i$ points in $\tilde{k}$-space represented in Fig.(3.3), [11].
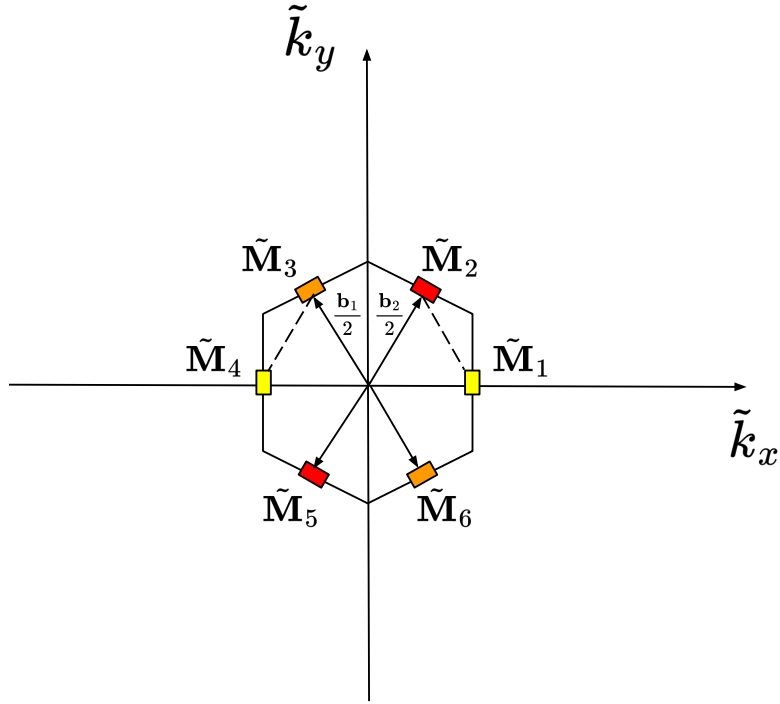
Figure 3.3: Possible positions of merge in $\tilde{\mathbf{k}}$-space. Equivalent points are indicated with the same color.

In fact, if $\mathbf{K}$ satisfies eq.(3.11), then also $-\mathbf{K}$ is a possible solution. In particular, for each Dirac point $\mathbf{K}$ there is always a non-equivalent one at $-\mathbf{K}$. When these two merge, their final position is the same up to a generic reciprocal lattice vector

$$\mathbf{K} = -\mathbf{K} + \mathbf{b} \quad , \ \mathbf{b} \in \text{reciprocal lattice} \quad . \tag{3.21}$$

Therefore the possible points of merge are located at $\frac{\mathbf{b}}{2}$ (or the origin if $\mathbf{K} = -\mathbf{K} = 0$). Within the first Brillouin zone these points are the ones indicated in Fig.(3.3).

As a final remark, we note that it is possible to obtain the expression for the shifted position of the Dirac points in the original $\mathbf{k}$-space by simply applying to the expressions in $\tilde{\boldsymbol{k}}$-space the opposite of the transformation (3.12):

$$\mathbf{k}_d = ((I + \hat{\epsilon})^T)^{-1}\tilde{\mathbf{k}}_d. \tag{3.22}$$

3.2 Review of Elasticity Theory for Solids

In order to analyse the properties of strained graphene, we need to know how its lattice structure gets affected by an external tension. Strain is in fact achieved by applying mechanical stress on a graphene sheet, therefore a description which relates stress and strain needs to be employed. This is provided by the theory of elasticity, that effectively describes how an homogeneous solid behaves under mechanical stress assumed to be small (elastic regime). For our purposes it will be sufficient to restrict the discussion to the two dimensional case.

We first begin by providing the definition of the strain tensor [19]. For that purpose let us consider an infinitesimal element of a 2D solid, as in figure (3.4).
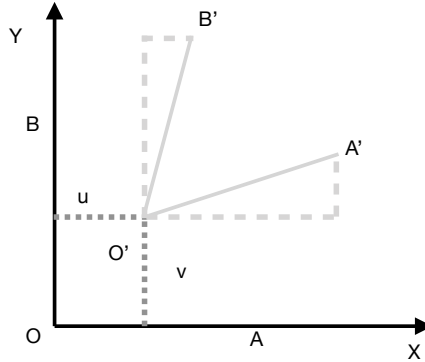

Figure 3.4: A general deformation of the infinitesiaml segments OA and OB. Adapted from [19].

A general deformation of the object can be described by the vector field:

$$\vec{\mathcal{U}} = \begin{pmatrix} u(x,y) \\ v(x,y) \end{pmatrix} \tag{3.23}$$

giving the displacement vector induced on each point of the body by the deformation, which, for the following discussion, we are going to assume to be small. In particular the displacement of point A along $\hat{x}$ is

$$u(A) = u(dx,0) = u(0,0) + \frac{\partial u}{\partial x}\Big|_{/(0,0)} dx. \tag{3.24}$$

A measure of strain along $\hat{x}$ can be defined as:

$$\epsilon_x := \frac{A'O'_x - AO_x}{AO_x} = \frac{(u + \frac{\partial u}{\partial x}dx + dx - u) - dx}{dx} = \frac{\partial u}{\partial x}. \tag{3.25}$$

In the previous expression, and in the following, the functions $u(x,y)$ and $v(x,y)$, as their derivatives, are understood to be evaluated at O if not specified otherwise.

Similarly along $\hat{y}$ we have

$$\epsilon_y := \frac{O'B'_y - OB_y}{OB_y} = \frac{\partial v}{\partial y} \tag{3.26}$$

These quantities are called normal strains, and they quantify linear elongation.

Let us now consider the deformation given by the change of the angle $B\hat{O}A$. The displacement of A along y is:

$$v(A) = v(dx, 0) = v + \frac{\partial v}{\partial x}dx \tag{3.27}$$

Therefore the angle α can be approximated as:

$$\alpha \approx tan(\alpha) = \frac{v + \frac{\partial v}{\partial x} - v}{dx + \frac{\partial u}{\partial x}dx} \approx \frac{\frac{\partial v}{\partial x}dx}{dx} = \frac{\partial v}{\partial x} \tag{3.28}$$

where in the first and third passage we have used respectively the assumption of small angular deformation and small strain along $\hat{x}$.

With similar calculations we also find

$$\beta = \frac{\partial u}{\partial y} \tag{3.29}$$

The two previous angles are used to define the shear strain as:

$$\gamma_{xy} = (\alpha + \beta) \tag{3.30}$$

which is the change of angle between the axis $\hat{x}$, $\hat{y}$.

Finally, the strain tensor is defined by

$$\hat{\epsilon} = \begin{pmatrix} \epsilon_x & \frac{1}{2}\gamma_{xy} \\ \frac{1}{2}\gamma_{xy} & \epsilon_y \end{pmatrix} \tag{3.31}$$

It is therefore symmetric by definition. We can also rewrite it explicitly in terms of the gradient of the displacement field as

$$\hat{\epsilon} = \frac{1}{2}(\nabla \mathcal{U} + (\nabla \mathcal{U})^T). \tag{3.32}$$

which makes the tensorial nature of $\hat{\epsilon}$ become evident.

Having defined the strain tensor, we can now describe how it relates to stress. Let us consider a two dimensional object, for simplicity of rectangular shape, and imagine to apply a tension $\hat{T}$ to it. We are going to examine two ways in which this can be done: one is to exert a normal tension, uniformly distributed over two opposite sides. The other is to apply the tension parallelly to the sides.
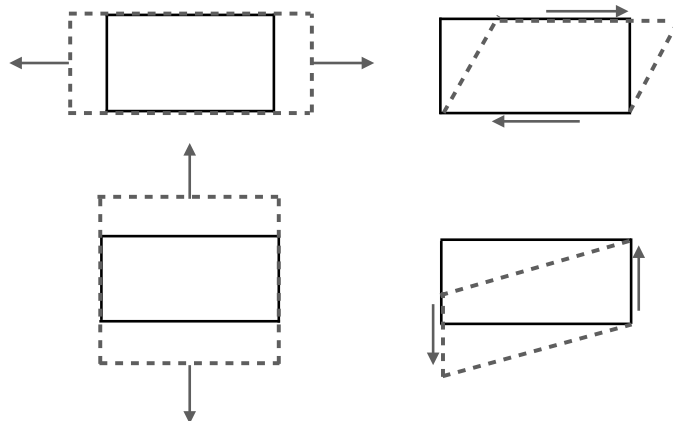

Figure 3.5: On the left is depicted normal strain, on the right shear strain.

The first scenario is described by Hook's law, that states the proportionality between stress and strain along the same direction:

$$\epsilon_i = \frac{1}{E}\sigma_i \tag{3.33}$$

where E is the Young modulus. Each of these elongations is accompanied by an additional induced transverse strain

$$\epsilon_i = -\nu\epsilon_j \quad , \quad i \perp j \tag{3.34}$$

with ν the Poisson's ratio of the material. Typically the value of ν is positive, resulting in a transverse contraction. A simple example of the latter effect can be observed by stretching a rubber band: its length will increase whereas the thickness will be simultaneously reduced. For graphene we have $\nu = 0.165$. Therefore considering for example a stress σ applied along $\hat{x}$, the strain tensor will have the form:

$$\hat{\epsilon} = \epsilon \begin{pmatrix} 1 & 0 \\ 0 & -\nu \end{pmatrix} \tag{3.35}$$

where $\epsilon = \frac{\sigma_x}{E}$ is our tunable parameter. This first scenario represents normal strain, a special case of uni-axial strain.

It is useful to also derive the form of the strain tensor in the case where a normal tension is still applied to the sides, as in the first case, but the edges of the 2D graphene sheet do not coincide with the coordinate axis.
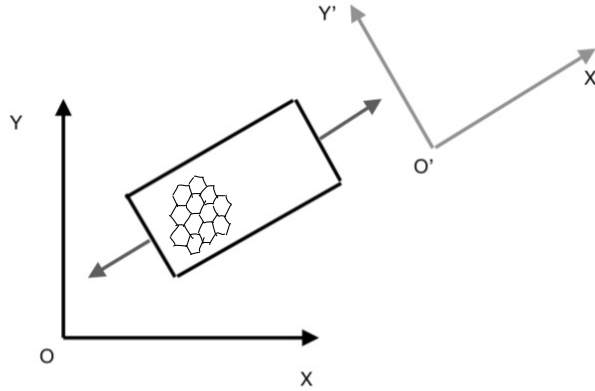

Figure 3.6: Uni-axial strain of generic angle. Notice that we keep the zig-zag direction of graphene always along $\hat{y}$ (before applying strain).

Let us consider it in a reference frame where the tension is directed along the new horizontal direction $\hat{x}'$. In these coordinates we will observe a strain along $\hat{x}'$ and a compression along $\hat{y}'$, therefore the strain tensor takes the form:

$$\hat{\epsilon}' = \epsilon \begin{pmatrix} 1 & 0 \\ 0 & -\nu \end{pmatrix}. \tag{3.36}$$

Obtaining its form in the original frame is simply achieved by a rotation [16]:

$$\hat{\epsilon}_{ij} = R(\theta)_{im} R(\theta)_{jn} \hat{\epsilon}'_{mn} = R(\theta) \cdot \hat{\epsilon}' \cdot R(\theta)^t = \epsilon \begin{pmatrix} \cos^2\theta - \nu \sin^2\theta & (1+\nu)\cos\theta\sin\theta \\ (1+\nu)\cos\theta\sin\theta & \sin^2\theta - \nu\cos^2\theta \end{pmatrix}$$
(3.37)

This will be useful in order to consider uni-axial strain along directions different than the ones of the coordinated axis.

We now turn to the scenario where the tension is applied parallelly to the sides. In particular by σ_{ij} we indicate a stress directed along $\hat{j}$, applied on the side whose external normal is $\hat{i}$. In the case of shear strain, this tensions come in pairs on opposite sides with opposite orientations. The two cases depicted on the right of Fig.(3.5) represent simple shear. It is important to note that simple shear also causes a rigid rotation on the object, which we ignore since we are only interested in deformations. We can also combine two simple shears as in Fig.(3.7) to obtain deformation with a null torque.
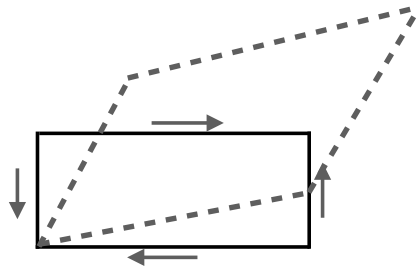

Figure 3.7: Pure shear strain.

It can be proven that pure shear and simple shear are equivalent in terms of deformations (modulo rigid rotations). Therefore in the following we are going to focus just on pure shear.

Applying shear stress produces an angle deformation according to the law

$$\gamma_{xy} = \frac{1}{G}\sigma_{xy}$$
(3.38)

with G the shear modulus. Finally the corresponding strain tensor has the form

$$\hat{\epsilon} = \epsilon \begin{pmatrix} 0 & 1 \\ 1 & 0 \end{pmatrix}.$$
(3.39)

3.3 Numerical Analysis

In the following we will test and verify the previous analytical calculations by means of numerical methods. In particular, we apply to the graphene structure uni-axial strain in different directions [16] as well as shear strain [6].

3.3.1 Uni-axial Strain

Uni-axial strain is the simplest possible strain patter, which consists of applying tension along a certain axis. As we have discussed in the previous section, for a generic direction of angle θ the strain tensor reads [16]

$$\hat{\epsilon} = \epsilon \begin{pmatrix} \cos^2 \theta - \nu \sin^2 \theta & (1 + \nu) \cos \theta \sin \theta \\ (1 + \nu) \cos \theta \sin \theta & \sin^2 \theta - \nu \cos^2 \theta \end{pmatrix} \tag{3.40}$$

As a first numerical analysis we explore the different directions of strain, and observe in which conditions the energy spectrum acquires a gap. Due to the rotational symmetry of the honeycomb lattice, it is sufficient to restrict the analysis to the angular interval $[0, \frac{\pi}{6}]$.

The numerical simulation for a given angle of strain θ has been performed as follows: the strain intensity is increased in steps of $d\epsilon$, and for each step the new position of the Dirac points is determined. This is done by Monte Carlo sampling a square centered at their position in the previous step, and looking for the new points that minimize the energy in the square. The critic strain has been determined as the first strain value for which the Dirac points disappear, i.e. their corresponding energy becomes sensibly different than 0. The result of the simulation is shown in figure (3.8). We can see that indeed a gap can be opened, with different strain thresholds depending on the direction.

Of particular relevance are the two special cases $\theta = 0$ (equivalent to $\frac{\pi}{3}$), and $\theta = \frac{\pi}{6}$ (equivalent to $\frac{\pi}{2}$), corresponding respectively to the armchair and zig-zag directions. These two scenarios appear to be opposed, as in the first the gap is never present, whereas the second corresponds to the most efficient gap opening direction, requiring the smallest strain threshold:

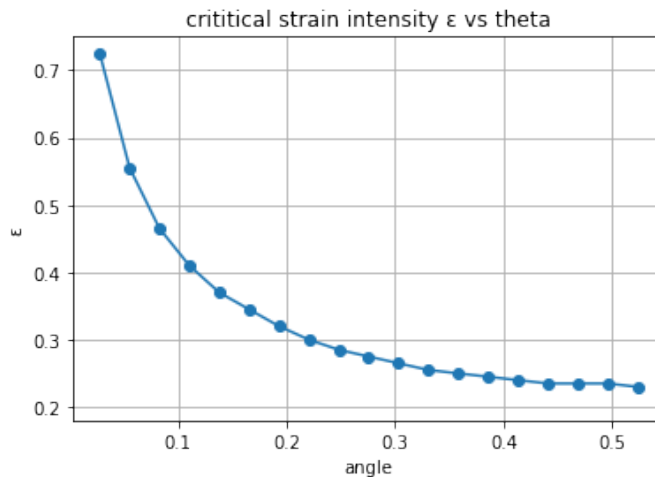$$\epsilon_{zig-zag} \approx 0.23. \tag{3.41}$$

Figure 3.8: Gap opening strain threshold as a function of direction.

Secondly, we observed how the Dirac points are affected by strain. Figure (3.12) shows the evolution of their position for increasing intensity ϵ in the special case of zig-zag strain. As we can see the Brillouin zone gets distorted, and concurrently the Dirac points drift away from its corners to finally merge [9].
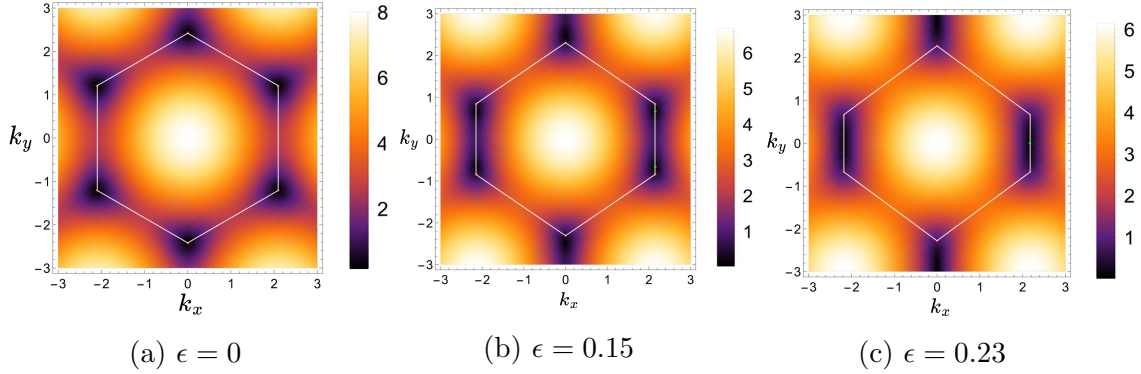

(a) $\epsilon = 0$ (b) $\epsilon = 0.15$ (c) $\epsilon = 0.23$

Figure 3.9: Merging of the Dirac points applying $\mathcal{Z}$ strain. The white contour denotes the first Brillouin zone, with the red points marking its corners. The Dirac points are indicated in green. The colors of the heat map encode the value of the energy band considered.

Figure(3.10b) specifically shows the evolution of the position of the Dirac points $\boldsymbol{k}_{d1}$ and $\boldsymbol{k}_{d6}$ both in $\mathbf{k}$ and $\tilde{\boldsymbol{k}}$ space.

(a) In $\mathbf{k}$ space.   (b) In $\tilde{\boldsymbol{k}}$ space.
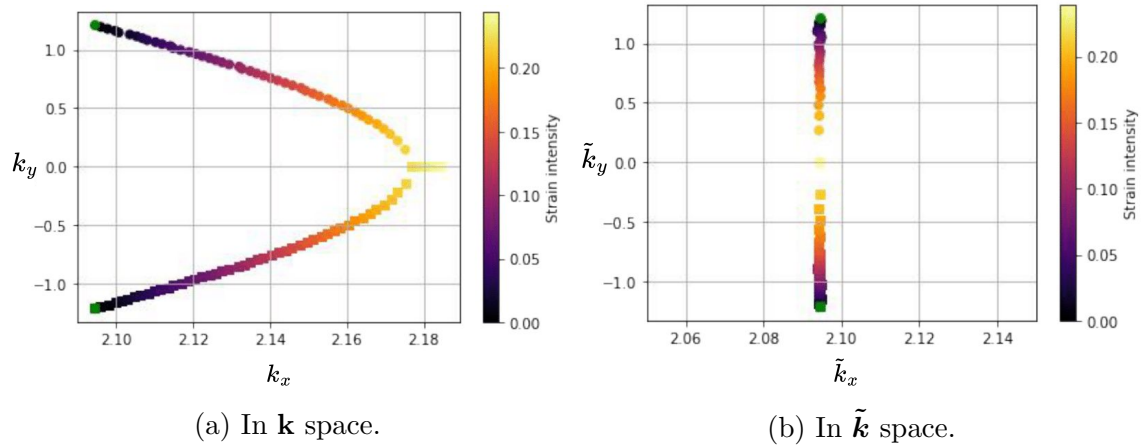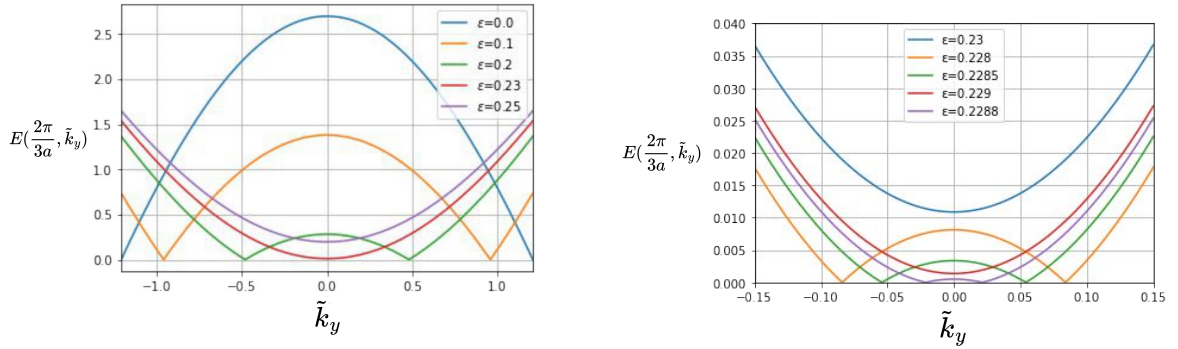
Figure 3.10: Evolution of the positions of $\boldsymbol{k}_{d1}$ and $\boldsymbol{k}_{d6}$ for an increasing $\mathcal{Z}$ strain intensity.

As already seen in paragraph (3.1.2), for a strain along $\mathcal{Z}$, $\boldsymbol{kd}_1$ and $\boldsymbol{kd}_6$ approach each other by moving along the axis $\tilde{k}_x = \frac{2\pi}{3a}$ in $\tilde{\boldsymbol{k}}$ space. The following figures show the profile of the upper energy band along the merging axis for increasing strain values.

(a) Energy profile along the merging axis with increasing $\mathcal{Z}$ strain.

(b) A zoom of the figure on the left.

Figure 3.11

On the other hand, in the case of $\theta = 0$ (armchair direction) the Dirac points drift away from each other and consequently the gap is not opened.

In the case where a generic strain direction is chosen, the Brillouin zone will undergo a different distortion, but the merging of in-equivalent Dirac points still occurs (although with different pairings), and simultaneously the gap is opened.
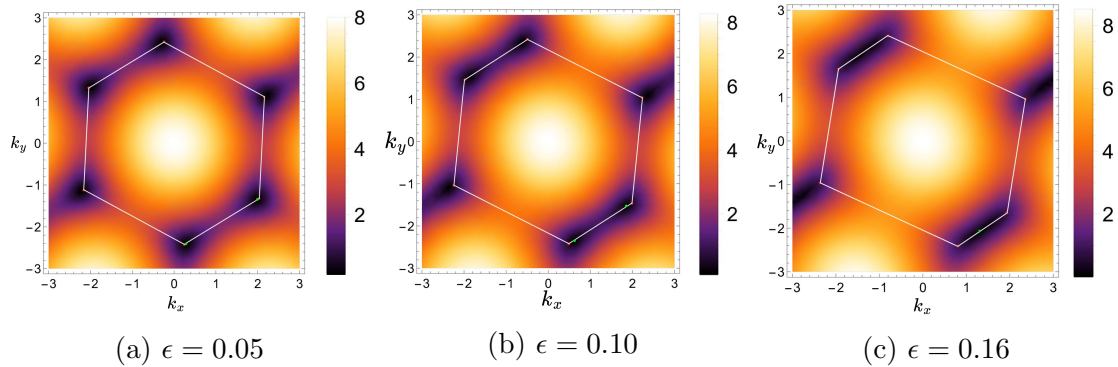
3.3.2   Shear Strain

We now turn to the case of shear strain [6] and repeat the same numerical analysis, as done for the uni-axial scenario. We will see that there are no conceptual differences with the previous case: in-equivalent Dirac points still merge, leading to the opening of a gap. However one difference can be observed in the value of the critic strain, which appears to be lower than the critic $\epsilon_{zig-zag}$.

The shear strain tensor reads:

$$\hat{\epsilon} = \begin{pmatrix} 0 & \epsilon \\ \epsilon & 0 \end{pmatrix} \tag{3.42}$$

We are going to consider only the case of $\epsilon > 0$. For $\epsilon < 0$ the results obtained are the same up to a global rotation. The following set of figures shows the energy heat map in the first Brillouin zone.

(a) $\epsilon = 0.05$

(b) $\epsilon = 0.10$

(c) $\epsilon = 0.16$

Figure 3.12: Merging of the Dirac points applying pure shear strain.

As anticipated, the Dirac points kd_6 and kd_5 merge. More specifically, the following figure shows the evolution of their position both in k and $\tilde{k}$ space.
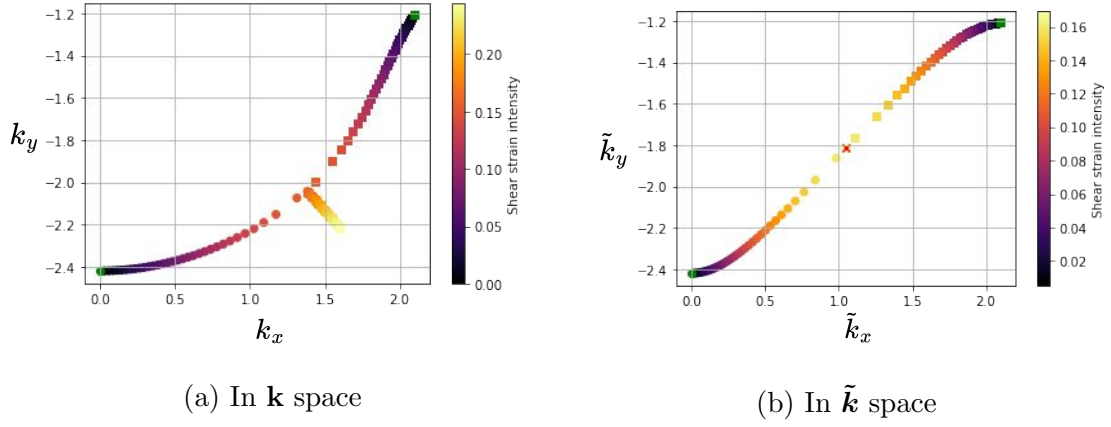
(a) In **k** space

(b) In $\tilde{\boldsymbol{k}}$ space

Figure 3.13: Evolution of the positions of $\boldsymbol{k}_{d5}$ and $\boldsymbol{k}_{d6}$ for an increasing shear strain.

The critic strain has been numerically determined to be

$$\epsilon_{shear} = 0.162, \tag{3.43}$$

which corresponds to a change in the angle between the axis $\hat{x}$ and $\hat{y}$ of approximately $9°$.

3.4   On the Merging of the Dirac Cones

The previous numerical results have highlighted the close connection, in the presence of strain, between the merge of in-equivalent Dirac points and the creation of a spectral bulk gap. In other words, it seems that the formation of the gap is always accompanied by the merging of Dirac cones. At first glance this appears to be a coincidence, determined by how the hopping parameters are tuned by strain. However we can give a simple interpretation of the mechanism as follows.

For simplicity, let us consider the case of uni-axial strain along $\mathcal{Z}$. As already seen, in $\tilde{\mathbf{k}}$ space the Dirac points k_{D1} and k_{D2} move vertically along $\tilde{k}_x = \frac{2\pi}{3a}$, to then meet on the $\tilde{k}_x$ axis.

The profiles of the positive and negative energy bands along that direction are respectively given by

$$E_{y\pm} = \pm \left| t_3 - 2t_1 \cos\left(\frac{\sqrt{3}\tilde{k}_y}{2}\right) \right|. \tag{3.44}$$
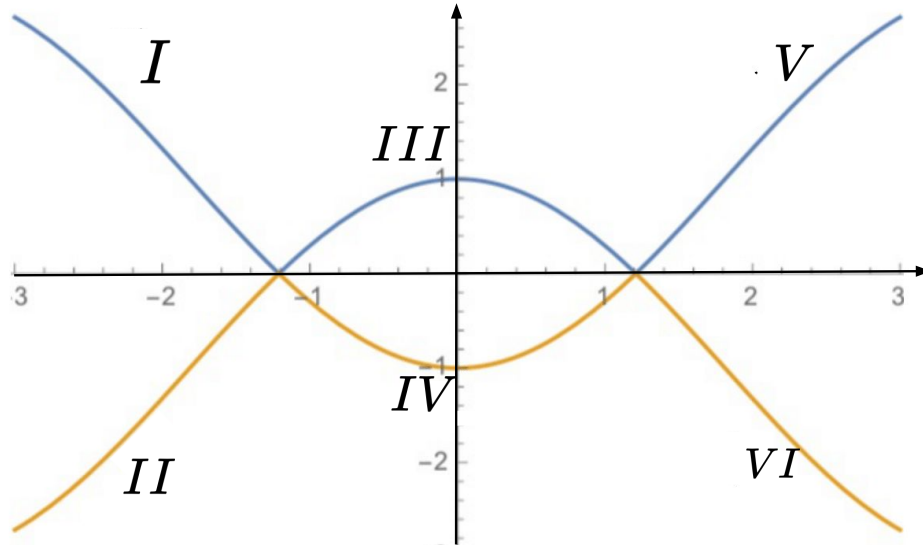
Figure 3.14: Energy profile along the direction of merge of the Dirac cones.

From the fig.3.14 we see that the branches labelled by I and IV correspond to different eigenvalues of the diagonalized Hamiltonian. However the derivative of the parabolic curve, obtained by sewing together I and IV, is always continuous at the point of junction between the two different bands. The same is true for the symmetric point, meaning that we can effectively treat the branches I, IV, V as a single band (and II, III, VI as well). Therefore, it becomes clear that the change in the hopping parameters induced by strain acts by moving the two parabolic curves vertically and changing their width. The only way to open a gap is then to pull the top parabolic band upwards, and the lower downwards, which also necessarily merges $\mathbf{k}_{d1}$ and $\mathbf{k}_{d2}$.

3.5   Low Energy Effective Hamiltonian

In section (1.2.1) we have seen that graphene exhibits an emergent Dirac theory in the low energy limit, with effective Hamiltonian of the form

$$H = \alpha q_x + \beta q_y \tag{3.45}$$

where α and β satisfy:

$$\{\alpha, \beta\} = 0 \quad , \quad \alpha^2 = \beta^2 \propto \mathbb{1}. \tag{3.46}$$

All the possible mass terms that, if introduced in the theory, produce an energy gap, are found in the form of sixteen terms that anti-commute with both α and β and square to the identity [2].

On the other hand, in the previous sections we have seen that strain can induce a gap in the energy spectrum of graphene as a result of the merging of non equivalent Dirac points. It is therefore natural to ask if the strain patterns considered are connected to any of those sixteen general mass terms of the effective Dirac Hamiltonian. In other words, the question we try to answer is: does the application of uni-axial or shear strain to the system modify the effective mass-less Dirac theory by introducing one (or a combination) of mass terms? To address the question we build the effective low energy theory for strained graphene. The procedure follows the same steps done for unstrained graphene (and kagomé), nevertheless we are going to remark its fundamental points.

Constructing a low energy theory consists in considering the situation where only low energy states are accessible by the system. If we properly set the chemical potential, these are momentum states close to the Dirac points:

$$|\mathbf{K}_d + \mathbf{q}\rangle \quad ; \quad |\mathbf{K}'_d + \mathbf{q}\rangle \tag{3.47}$$

where $\mathbf{K}_d$, $\mathbf{K}'_d$ are two generic in-equivalent valleys, and $\mathbf{q}$ is to be taken small.

In particular we are interested in the case where the Dirac points are already merged ($\mathbf{K}_d = \mathbf{K}'_d := \mathbf{M}$) because this is when the gap is created. In that regime, since the two points coincide, the valley index is not a good degree of freedom anymore. It follows that the spinless effective low energy Hamiltonian is just the expansion of the Block Hamiltonian around the point of merge $\mathbf{M}$:

$$H = \begin{pmatrix} 0 & \Delta_{\mathbf{M}+\mathbf{q}} \\ \Delta^*_{\mathbf{M}+\mathbf{q}} & 0 \end{pmatrix} \tag{3.48}$$

with $\Delta_{\mathbf{M}+\mathbf{q}}$ being the linear expansion of $\Delta(\mathbf{k}) = \sum_j t(\boldsymbol{\delta}_j)e^{i\mathbf{k}\cdot(I+\hat{\epsilon})\boldsymbol{\delta}_j}$ around $\mathbf{M} + \mathbf{q}$ (with $\mathbf{q}$ a small momentum deviation).

Now, in order to detect the presence of mass terms introduced by the strain, we ought to bring this Hamiltonian in the form of a mass-less Dirac Hamiltonian plus the supposed constant mass term. Looking at the form of the matrix, we can in general decompose it as

$$H = \begin{pmatrix} 0 & \Delta_{\mathbf{M}+\mathbf{q}} \\ \Delta^*_{\mathbf{M}+\mathbf{q}} & 0 \end{pmatrix} \sim (aq_x + bq_y)\sigma_1 + (cq_x + dq_y)\sigma_2 + m_1\sigma_1 + m_2\sigma_2 \tag{3.49}$$

where σ_1, σ_2 are Pauli matrices as usual. To bring eq.(3.49) in the usual Dirac form, it seems natural to relabel the momentum variables, so that we get

$$H \sim \tilde{q}_x\sigma_1 + \tilde{q}_y\sigma_2 + m_1\sigma_1 + m_2\sigma_2 \tag{3.50}$$

However this would yield to a contradictory result: this is in fact a mass-less Dirac Hamiltonian, as mass terms would only be proportional to σ_z in this case. But on the contrary the spectrum shows a gap after the Dirac points have merged. In reality, the change of momentum variables performed is not allowed. The reason is that the energy dispersion, after merging, becomes linear in one momentum direction and quadratic in the normal one. In the case of strain along $\mathcal{Z}$ it is linear along q_x and quadratic along q_y, such that terms in q_y will not show up in the linear expansion of eq.(3.49), and we have instead:

$$\begin{pmatrix} 0 & \Delta \\ \Delta^* & 0 \end{pmatrix}_{\mathcal{Z}} \sim aq_x\sigma_1 + cq_x\sigma_2 + m_1\sigma_1 + m_2\sigma_2 \tag{3.51}$$

It is apparent now why the previous relabel of momenta is forbidden, because degenerate. Moreover in the case of a generic strain pattern, the combination of q_x and q_y coupling to the two Pauli matrices will be the same, such that we can do a rotation of coordinates and end up in the same situation (valid for $\mathcal{Z}$ strain) described by (3.51).

The fact that the effective theory couples the Pauli matrices to the same momentum direction has important implications. For such a theory it is in fact still true that the mass terms are the ones anti-commuting with the matrices coupled to the momenta (here σ_1, σ_2). However there are additional ones, and in particular both σ_1 and σ_2 can open a gap in this case. As an example, let us consider the case of σ_1. If we add such term to a usual massless Dirac theory:

$$H = \sigma_1 q_x + \sigma_2 q_y + m\sigma_1 \tag{3.52}$$

then the resulting energy spectrum is

$$E = \pm\sqrt{(q_x + m)^2 + q_y^2} \tag{3.53}$$

which remains gapless as we can see by shifting coordinates(indeed in this case the effect is to simply shift the position of the Dirac point). However assuming an Hamiltonian of the type (3.51):

$$H = \sigma_1 q_x + \sigma_2 q_x + m\sigma_1 \tag{3.54}$$

the spectrum is

$$E = \pm\sqrt{(q_x + m)^2 + q_x^2} \tag{3.55}$$

which now exhibits a gap.

This shows that the mechanism by which the gap is opened with the strain is not the expected one, namely the introduction of usual mass terms in the Dirac theory. But rather a modification of the Dirac theory itself, by coupling the same momentum to both Pauli matrices, which results into the constant terms introduced by strain being good gap terms.

Chapter 4

Strained Kagomé

In the previous chapter we have studied the effects of uni-axial and shear strain applied to the lattice structure of graphene. The main effect observed was the merge of in-equivalent Dirac points, with the consequent opening of a gap in the spectrum. Therefore strain revealed to be a viable method to induce a phase transition from a semimetal to insulator in the material. On the other hand, as we have seen, the kagomé lattice presents many similarities with graphene, the most important being the emergent Dirac structure in the low energy limit. It is therefore natural to ask if strain could induce a gap also in its spectrum. In this chapter we address this question, following a similar approach as in the graphene case.

4.1 Numerical Analysis

We generalize to the kagomé lattice the analysis done in the graphene case. The discussion follows the same conceptual steps, which we briefly recall. Elastic strain alters the lattice bond lengths, resulting in a modulation of the hopping parameters according to the law

$$t(\boldsymbol{\delta}') = t_0 e^{-g(\frac{|\boldsymbol{\delta}'|}{a}-1)} \tag{4.1}$$

where as usual $\boldsymbol{\delta}' = (I + \hat{\epsilon})\boldsymbol{\delta}$, and g is the Grünisen parameter. In accordance with the literature we assume $g = 1$ [10]. The tight binding model is therefore modified as

$$\mathbf{H} = -\sum_{<i,j,l>,\sigma} (t_{ij} a_{i,\sigma}^\dagger b_{j,\sigma} + t_{il} a_{i,\sigma}^\dagger c_{l,\sigma} + t_{jl} b_{j,\sigma}^\dagger c_{l,\sigma} + h.c.), \tag{4.2}$$

which, following the same steps done in Chapter 2, can be rewritten after some calculations as

$$\mathbf{H} = -2 \sum_{k,\sigma} \Psi_\sigma^\dagger(\mathbf{k}) \begin{pmatrix} 0 & t_{AB} \cos(\mathbf{k} \cdot \boldsymbol{\delta}'_{AB}) & t_{13} \cos(\mathbf{k} \cdot \boldsymbol{\delta}'_{AC}) \\ t_{AB} \cos(\mathbf{k} \cdot \boldsymbol{\delta}'_{AB}) & 0 & t_{BC} \cos(\mathbf{k} \cdot \boldsymbol{\delta}'_{BC}) \\ t_{13} \cos(\mathbf{k} \cdot \boldsymbol{\delta}'_{AC}) & t_{BC} \cos(\mathbf{k} \cdot \boldsymbol{\delta}'_{BC}) & 0 \end{pmatrix} \Psi_\sigma(\mathbf{k}) =$$

$$= \sum_{k,\sigma} \Psi_\sigma^\dagger(\mathbf{k}) H(\mathbf{k}) \Psi_\sigma(\mathbf{k}) \tag{4.3}$$

The energy eigenvalues can then be determined by numerical diagonalization of the Block Hamiltonian $H(\mathbf{k})$.

We start the numerical analysis by first considering once again uni-axial strain. The strain tensor has the usual form of eq.(3.40), where ν is now the kagomé Poisson's ratio. For the purpose of our simulations, we assumed the same value as for

graphene

$$\nu = 0.165. \tag{4.4}$$

As already mentioned, the kagomé lattice presents a six fold symmetry. it follows that, when applying uni-axial strain, it is sufficient to explore the directions in the angular interval $[0, \frac{\pi}{3}]$. In order to asses the presence of a spectrum gap, we constructed the density of states for the strained system. This was obtained by Monte Carlo sampling the first Brillouin zone and numerically diagonalizing the Hamiltonian. Moreover, in order to exclude the possibility that the gap is not observed due to a bad choice of the parameters in the model, we extended our analysis to a range of strain intensities with all probability beyond the material elastic failure.

Fig.(4.1) depicts the density of states in absence of strain, whereas in the following figures we show as an example some cases corresponding to different strain patterns and intensities.
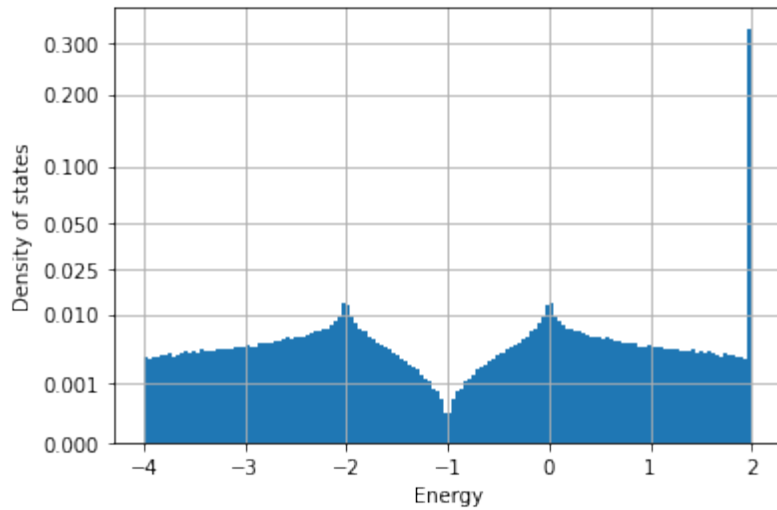

Figure 4.1: Density of states of the kagomé lattice in the unstrained case. In this particular case a non linear y scale has been used in order to better visualize the density profile.
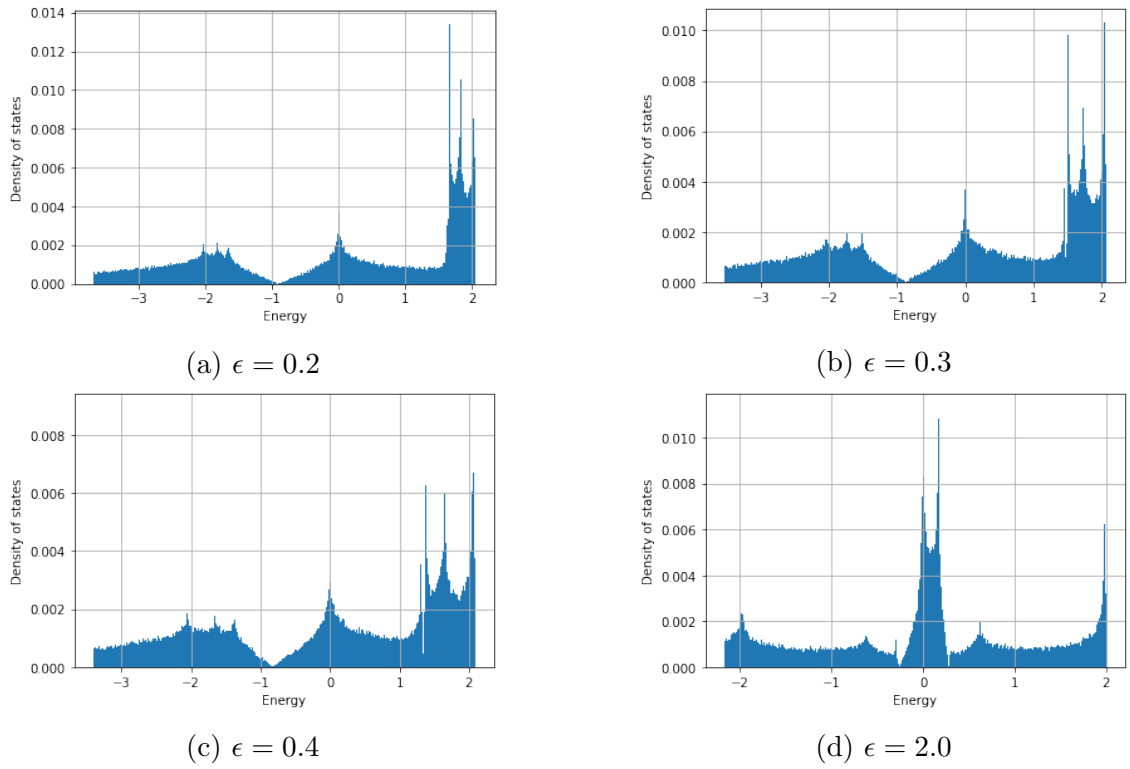
(a) $\epsilon = 0.2$

(b) $\epsilon = 0.3$

(c) $\epsilon = 0.4$

(d) $\epsilon = 2.0$

Figure 4.2: Uni-axial strain in direction $\theta = \frac{\pi}{12}$ applied to the kagomé lattice for increasingly intensity ϵ.

(a) $\epsilon = 0.2$

(b) $\epsilon = 0.3$
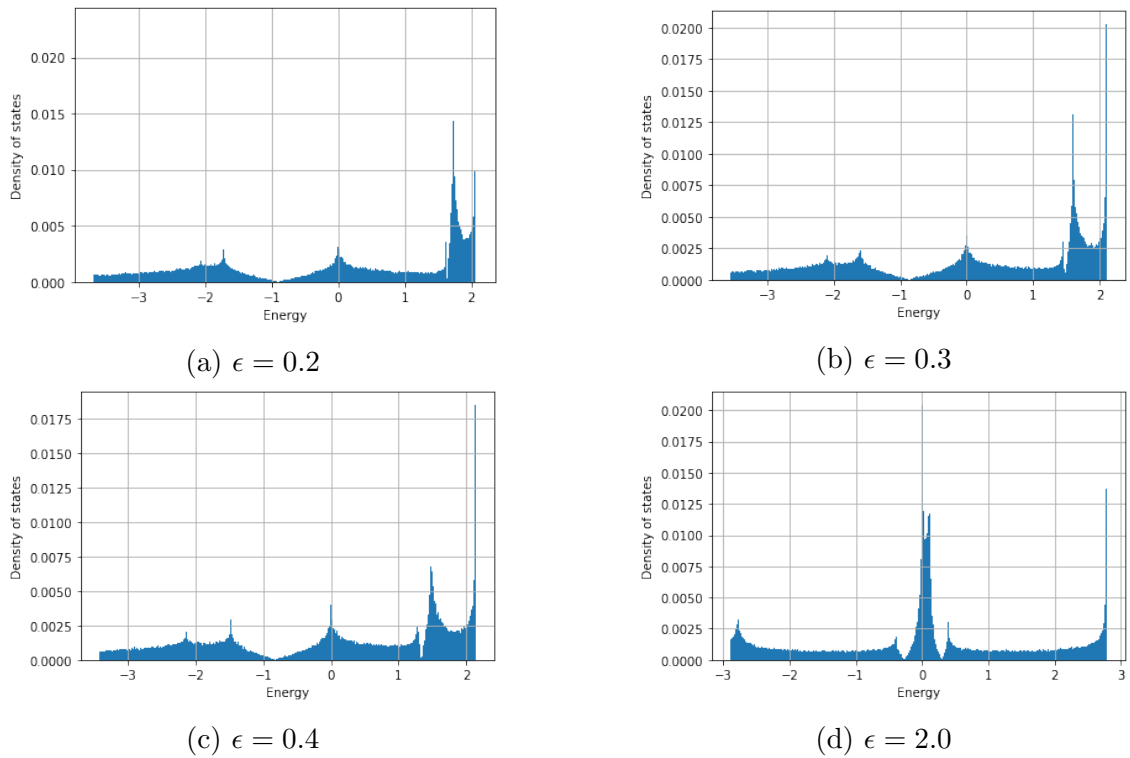
(c) $\epsilon = 0.4$

(d) $\epsilon = 2.0$

Figure 4.3: Uni-axial strain in direction $\theta = \frac{\pi}{6}$ applied to the kagomé lattice for increasingly intensity ϵ.

As it appears clearly from the plots, no sensible gap is opened in the spectrum. Moving on to the case of shear strain, the strain tensor has the form as in

eq.(3.42). The results are shown in Fig.(4.4), and are no different from the uni-axial scenario.
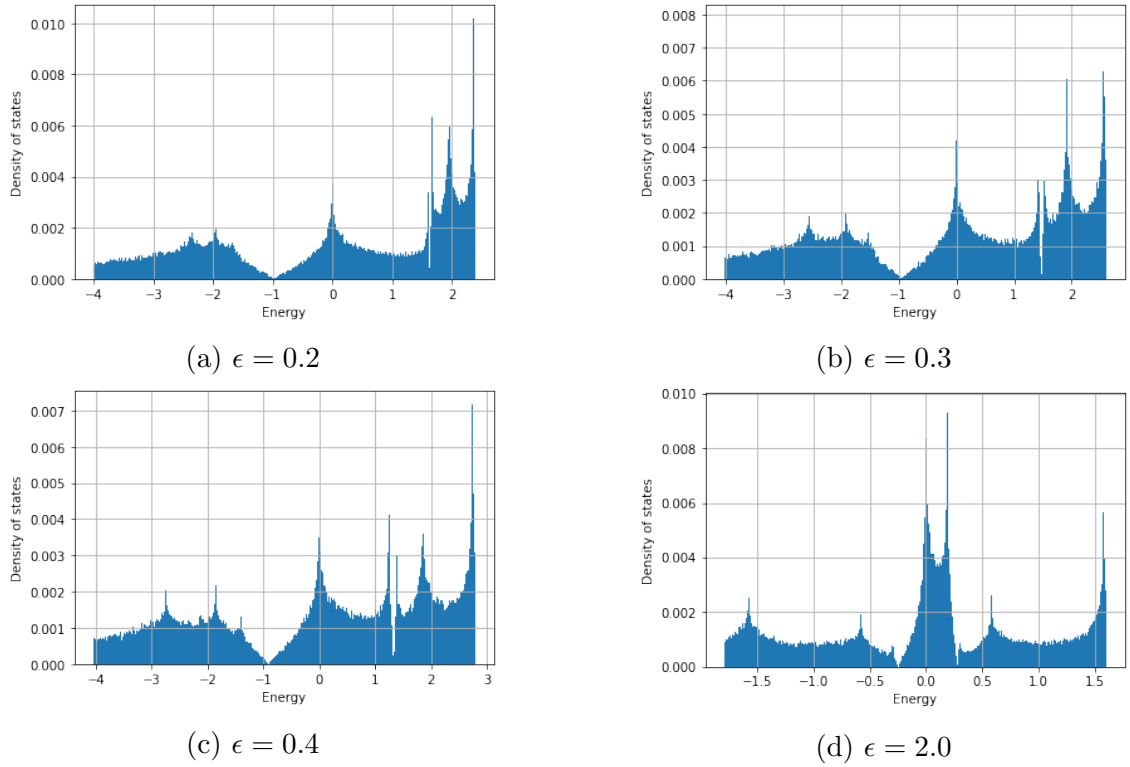

(a) $\epsilon = 0.2$ (b) $\epsilon = 0.3$

(c) $\epsilon = 0.4$ (d) $\epsilon = 2.0$

Figure 4.4: Shear strain applied to the kagomé lattice with increasingly intensity ϵ.

In all of the cases considered, we observe a progressive deformation of the flat band, which acquires ripples. Concurrently the middle band becomes progressively flat, producing a high peak of states at intermediate energy values for higher values of strain intensity. However no gap has been observed applying uni-axial and shear strain.

Chapter 5

Conclusions

In this thesis we have started by reviewing the graphene tight-binding model and in particular the emergent Dirac Hamiltonian arising from the low energy expansion. That served as example and guideline to extend the discussion to the kagomé lattice, a novel two-dimensional material that shares many similarities with graphene. In particular the former is also characterized by the presence of an underlying Dirac theory, which we have explicitly extracted. To do that the additional step of decoupling the flat band present in the spectrum was necessary, compared to the graphene case where only an expansion around the Fermi points is needed.

We have then analyzed the possible ways to induce a bulk gap in the kagomé spectrum. This has lead to a list of sixteen instabilities corresponding to the mass terms of the Dirac theory. Moreover we have proceeded to classify this list of mass terms based on the symmetries of the system, that can be either preserved or broken when introducing them. For that purpose it revealed to be crucial the observation that the equivalence between the Dirac points was not manifest in the form of the Block Hamiltonian. In fact that required the introduction of a Gauge transformation to reinforce the periodic boundary conditions in the theory, and restore the invariance of the model under equivalent valley choices.

In the second part of the thesis we have combined the previous tight-binding description with the linear theory of elasticity in order to introduce in the model lattice deformations. In particular we have considered distortion patters that were preserving the translation invariance of the system, such as uni-axial and shear strain. The effect of strain has been first analyzed in graphene, with a special focus on the modifications induced on the structure of the Dirac cones. In accordance with the literature, the main effects observed were the merge of in-equivalent Dirac points, with the consequent generation of a spectral gap. In the uni-axial case, different directions correspond to different intensity thresholds in order to achieve the collision of the Dirac points.

Motivated by the fact that strain has been shown to be a viable way to engineer a gap in graphene, we investigated its connection with the general mass terms of the Dirac theory. However we have seen that the mechanism by which strain acts to generate the gap is different from an effective introduction of one of the 16 possible masses of the Dirac theory. In fact it leads to a modification of the low energy model itself, by coupling the two anti-commuting objects present in the Dirac Hamiltonian (specifically the Pauli matrices σ_x and σ_y) to the same momentum component. As a result, the condition that has to be satisfied in order have a gap in the spectrum is relaxed, and the terms introduced by strain become good gap terms despite not being mass terms in the usual sense.

Finally we applied strain also to the kagomé lattice to see if the induced effects were comparable to the ones observed in graphene. However, for the particular strain patterns that we employed, no spectral gap was observed. We concluded that uni-axial and shear strain do not seem to be viable methods to tune the electronic properties of the kagomé lattice by generating a gap .

Bibliography

[1] Neil W. Ashcroft and N. David Mermin. *Solid State Physics (eighth edition)*. Cengage Learning, 2011.

[2] Claudio Chamon et al. "Masses and majorana fermions in graphene". In: *Physica Scripta* T146.014013 (2012).

[3] Ching-Kai Chiu et al. "Classification of topological quantum matter with symmetries". In: *Reviews of modern physics* 88.035005 (2016).

[4] Hasna Chnafa et al. "Effect of strain on band engineering in gapped graphene". In: *The European Physical journal B* 94.39 (2021).

[5] Riccardo Ciola et al. "Chiral symmetry breaking through spontaneous dimerization in kagomé metals". In: *Physical Review B* 104.245138 (2021).

[6] Giulio Cocco, Emiliano Cadelano, and Luciano Colombo. "Gap opening in graphene by shear strain". In: *Physical Review B* 81.241412(R) (2010).

[7] M. I. Katsnelson, K. S. Novoselov, and A. K. Geim. "Chiral tunnelling and the Klein paradox in graphene". In: *Nature Physics* 2 (2006), pp. 620–625.

[8] Charles Kittel. *Introduction to solid state physics (eighth edition)*. Wiley, 2004.

[9] Cui-Lian Li. "New position of Dirac points in the strained graphene reciprocal lattice". In: *AIP Advances* 4.087119 (2014).

[10] Tianyu Liu. "Strain-induced pseudomagnetic field and quantum oscillations in kagome crystals". In: *Physical Review B* 102.045151 (2020).

[11] G. Montambaux et al. "Merging of Dirac points in a two-dimensional crystal". In: *Physics Review B* 80.153412 (2009).

[12] A. H. Castro Neto et al. "The electronic properties of graphene". In: *Reviews of Modern Physics* 81.109 (2009).

[13] K. S. Novoselov et al. "Electric Field Effect in Atomically Thin Carbon Films". In: *Science* 306 (2004), pp. 666–669.

[14] M. Oliva-Leyva and Gerardo G. Naumis. "Generalizing the Fermi velocity of strained graphene from uniform to nonuniform strain". In: *Physics Letters A* 379.40-41 (2015), pp. 2645–2651.

[15] M. Oliva-Leyva and Gerardo G. Naumis. "Understanding electron behavior in strained graphene as a reciprocal space distortion". In: *Physical Review B* 88.085430 (2013).

[16] Vitor M. Pereira and Casto Neto. "Tight-binding approach to uniaxial strain in graphene". In: *Physical Review B* 80.045401 (2009).

[17] J.J. Sakurai and Jim Napolitano. *Modern Quantum mechanics (Second edition)*. Pearson, 2011.

[18]   CChen Si, Zhimei Sun, and Feng Liu. "Strain engineering of graphene: a review". In: *Nanoscale* 8.3207 (2016).

[19]   S. Timoshenko and J.N. Goodier. *Theory of elasticity (Second edition)*. McGraw-Hill Book company, 1951.

[20]   Binghai Yan and Claudia Felser. "Topological Materials: Weyl Semimetals". In: *Annual Reviews* 8 (2017), pp. 337–354.